Global gyrokinetic study of shaping effects on electromagnetic modes at NSTX aspect ratio with ad hoc parallel magnetic perturbation effects

A. Y. Sharma,[1, a)] M. D. J. Cole,[1] T. Görler,[2] Y. Chen,[3] D. R. Hatch,[4] W. Guttenfelder,[1] R. Hager,[1] B. J. Sturdevant,[1] S. Ku,[1] A. Mishchenko,[5] and C. S. Chang[1]

[1)] *Princeton Plasma Physics Laboratory, P.O. Box 451, Princeton, NJ 08543-0451, USA*

[2)] *Max Planck Institute for Plasma Physics, Boltzmannstr. 2, 85748 Garching, Germany*

[3)] *Department of Physics, University of Colorado at Boulder, 390 UCB, Boulder, Colorado 80309, USA*

[4)] *Institute for Fusion Studies, University of Texas at Austin, 1 University Station, C1500, Austin, Texas 78712, USA*

[5)] *Max Planck Institute for Plasma Physics, D-17491 Greifswald, Germany*

(Dated: 19 January 2023)

Plasma shaping may have a stronger effect on global turbulence in tight-aspect-ratio tokamaks than in conventional-aspect-ratio tokamaks due to the higher toroidicity and more acute poloidal asymmetry in the magnetic field. In addition, previous local gyrokinetic studies have shown that it is necessary to include parallel magnetic field perturbations in order to accurately compute growth rates of electromagnetic modes in tight-aspect-ratio tokamaks. In this work, the effects of elongation and triangularity on global, ion-scale, linear electromagnetic modes are studied at NSTX aspect ratio and high plasma β using the global gyrokinetic particle-in-cell code XGC. The effects of compressional magnetic perturbations are approximated via a well-known modification to the particle drifts that was developed for flux-tube simulations [N. Joiner et al., Phys. Plasmas **17**, 072104 (2010)], without proof of its validity in a global simulation, with the gyrokinetic codes GENE and GEM being used for local verification and global cross-verification. Magnetic equilibria are reconstructed for each distinct plasma profile that is used. Coulomb collision effects are not considered. Within the limitations imposed by the present study, it is found that linear growth rates of electromagnetic modes (collisionless microtearing modes and kinetic ballooning modes) are significantly reduced in a high-elongation and high-triangularity NSTX-like geometry compared to a circular NSTX-like geometry. For example, growth rates of kinetic ballooning modes at high-β are reduced to the level of that of collisionless trapped electron modes.

[a)]Electronic mail: asharma@pppl.gov

I. INTRODUCTION

Spherical tokamaks, such as the National Spherical Torus Experiment[1] (NSTX), its Upgrade[1,2] (NSTX-U), the Mega Ampere Spherical Tokamak[3] (MAST), and its Upgrade[4] (MAST Upgrade), could possibly be an attractive approach to magnetic fusion energy due to their high normalized plasma pressure and high bootstrap current fraction. In order to make experimental progress as efficiently as possible, numerical studies based on gyrokinetic[5] equations can be helpful.

In this study, we use the global gyrokinetic particle-in-cell (PIC) code XGC[6] to study the effects of plasma shaping on electromagnetic mode stability in low-aspect-ratio tokamaks, emphasizing the global nature of ion-scale modes, as well as a model that is presently available for the inclusion of compressional magnetic perturbation effects. Most of the previous gyrokinetic studies on shaping effects at tight aspect-ratio have been studied either with flux-tube codes[7–9] or with global codes without compressional magnetic perturbation effects,[10] while the strongly varying magnetic field strength and curvature may imply importance of both the global and compressional effects. The importance of compressional magnetic perturbation effects for tight-aspect-ratio plasmas is demonstrated in Refs. 11–15.

XGC is capable of performing global total-f electromagnetic gyrokinetic simulations of the whole tokamak plasma volume from the magnetic axis to the material wall. Only the δf simulation capability[16] is used in this work, and the scrape-off layer is not simulated. The total-f electromagnetic gyrokinetic simulation capability for the whole plasma volume will be reported elsewhere.[17]

While compressional modes are routinely included in local gyrokinetic simulations, a global gyrokinetic simulation that includes compressional modes is difficult to perform,[18,19] especially for a tight-aspect-ratio tokamak plasma. Instead, we utilize the well-known approximation that modifies the ∇B-drift.[7,13,18,20–24] This approximation has been verified with flux-tube simulations, as described in Section III, but no strict verification comparing global simulations with and without magnetic parallel fluctuations and correspondingly adjusted drifts has yet been performed. The reason for this is the lack of available global gyrokinetic codes that include $\delta B_{\parallel}$. For example, the local version of the gyrokinetic code GENE[25] includes $\delta B_{\parallel}$, however, at the time of writing, the development of $\delta B_{\parallel}$ in the global version of GENE has not yet been completed. In addition, while the gyrokinetic code GTC[19] includes

Mode	Type	Diamagnetic direction	Parity	Driven by	Stabilized by
ITG	ES/EM	Ion	Ballooning	∇T_i	β
KBM	EM	Ion	Ballooning	α	$\beta < \beta_\mathrm{crit}$
CTEM	ES	Electron	Ballooning	$\nabla T_\mathrm{e}, \nabla n$	Collisions
CMTM	EM	Electron	Tearing	β, ∇T_e	$\beta < \beta_\mathrm{crit}$

TABLE I. Various properties[8,30] of the collisionless electrostatic (ES) and electromagnetic (EM) ion-scale modes considered in this work, where $\nabla T_\mathrm{i,e}$ and ∇n are the ion and electron temperature and density gradients, respectively, β and β_crit are the normalized plasma pressure and its critical value,[8] respectively, $\alpha = -2\mu_0 q^2 R_0 \nabla P / B_0^2$ is the normalized pressure gradient, μ_0 is the vacuum magnetic permeability, R_0 is the tokamak major radius, P is the plasma pressure, and B_0 is the magnetic field strength on axis.

$\delta B_\parallel$, it is presently only available for fluid electrons (and some of the approximations used in the equations may not be valid for NSTX). Thus, this remains a caveat to the results of the present study.

We consider only collisionless ion-scale modes in this work, such as ion temperature gradient modes (ITGs),[26] kinetic ballooning modes (KBMs),[11] collisionless trapped electron modes (CTEMs),[27] and collisionless microtearing modes (CMTMs).[28,29] For convenience, we summarize some of the properties of these modes in Table I and, in addition, refer the reader to References 8 and 30. All of these modes have ballooning parity, except for MTMs, which have tearing parity. Modes with ballooning parity have a perturbed electrostatic potential along a field line that is an even function of the poloidal angle, and a perturbed parallel magnetic potential along a field line that is an odd function of the poloidal angle. Modes with tearing parity have the opposite symmetry.

The remainder of this paper is organized as follows. In order to properly take into account stabilizing, finite-pressure, "drift-reversal" effects,[13,18,31] we use profile-consistent magnetic equilibria throughout this work. This is described in Section II. Presently, there are both explicit[16] and implicit[32] numerical scheme options in XGC that are capable of electromagnetic simulations. We use the explicit option throughout this work. We present local verification and global cross-verification of an approximation for the inclusion of compressional magnetic perturbation effects in Section III. We then apply these developments

to study electromagnetic mode stabilization by shaping effects at NSTX aspect ratio and high plasma β using XGC. This is described in Section IV. Finally, we draw conclusions in Section V.

II. USE OF PROFILE-CONSISTENT MAGNETIC EQUILIBRIA

Performing scans over the normalized plasma pressure parameter β allows for the study of the transition from electrostatic to electromagnetic modes. As such, these scans have previously been used in the cross-verification of global electromagnetic gyrokinetic codes.[16,32,33] The usual convention when performing such scans is to use a fixed magnetic equilibrium and vary β either by scaling the input plasma density profile, or by scaling β in the Ampère equation. Such a convention is reasonable for the purpose of code cross-verification, however, for the purpose of physics studies, the assumption of a fixed magnetic equilibrium may not be valid. This is because changes in plasma pressure result in changes to the Shafranov shift, which, in turn, affects mode stability. Therefore, in order to obtain higher-fidelity stability studies, profile-consistent magnetic equilibria are used in this work. That is to say, the magnetic equilibrium is reconstructed at each value of β so that it is consistent with the input plasma profiles.

The 3D magnetohydrodynamic equilibrium solver code VMEC[34] is used to generate magnetic equilibria. The inputs to VMEC are given in terms of various geometry, resolution, and convergence parameters, as well as the rotational transform $\iota(\rho)$ and pressure $P(\rho)$ in terms of the normalized toroidal magnetic flux ρ, and the total enclosed toroidal magnetic flux Φ.

We consider axisymmetric and up-down symmetric magnetic geometries in this study. The geometry of an axisymmetric magnetic equilibrium is specified by the geometry of the boundary magnetic surface corresponding to the minor radius a of the tokamak poloidal cross-section as[35]

$$R(\theta) = R_0 + a\cos\left(\theta + \delta\sin\theta\right),$$
$$z(\theta) = \kappa a\sin\theta,$$

where R and z are the major radius and elevation coordinates, respectively, within a cylin-

drical coordinate system, R_0 is the major radius, θ is the poloidal angle coordinate,

$$\delta = \frac{R_0 - R_{z_{\max}}}{a}$$

is the up-down-symmetric triangularity, $R_{z_{\max}}$ is the value of R at $z_{\max}$, $z_{\max}$ is the maximum elevation of the boundary magnetic surface, and

$$\kappa = \frac{z_{\max} - z_{\min}}{2a}$$

is the elongation. The input to VMEC is given in terms of the Fourier representation of $R(\theta)$ and $z(\theta)$. We choose to keep both the rotational transform and the boundary of the magnetic equilibrium fixed when varying β.

The remaining stages of the workflow are to convert the VMEC output to G EQDSK format using the MConf[36] tool, and to convert the G EQDSK format to EQD format using XGC.

III. AN APPROXIMATION FOR THE INCLUSION OF COMPRESSIONAL MAGNETIC PERTURBATION EFFECTS

A. Local verification

Global gyrokinetic simulations of magnetic fusion plasmas usually neglect the effects of compressional magnetic perturbations, that is, the parallel component of the perturbed magnetic field is chosen to be zero, $\delta B_\parallel = 0$. Compressional magnetic perturbations may be included in global gyrokinetic simulations via standard[19] and extended[37–40] gyrokinetic orderings, although doing so introduces additional complexity and expense relative to standard global gyrokinetic schemes.[18,19] Alternatively, the effects of compressional magnetic perturbations may be approximated by modifying the ∇B-drift[7,13,18,20–24]. This approximation has previously been shown to give excellent agreement with a full $\delta B_\parallel$ model for certain cases at conventional[21] and high[18] aspect ratio.

We have verified this approximation with the Cyclone Base Case[41] (CBC) using the local version of GENE. We choose to use the local version of GENE because it has the capability to compare a full $\delta B_\parallel$ model against an approximate $\delta B_\parallel$ model, while XGC does not yet have this capability.

The electromagnetic gyrokinetic equations[25] solved by GENE take the ∇B-drift to be

$$\begin{aligned} v_{\nabla B_0} &= \frac{1}{\Omega}\hat{\boldsymbol{b}} \times \frac{v_\perp^2}{2}\frac{\boldsymbol{\nabla} B_0}{B_0} \\ &= \frac{1}{\Omega}\hat{\boldsymbol{b}} \times \frac{v_\perp^2}{2}\left[(\hat{\boldsymbol{b}}\cdot\boldsymbol{\nabla})\hat{\boldsymbol{b}} - \frac{4\pi}{B_0^2}\boldsymbol{\nabla} p\right], \\ \hat{\boldsymbol{b}} &= \frac{\boldsymbol{B}_0}{B_0}, \\ B_0 &= |\boldsymbol{B}_0|, \end{aligned} \tag{1}$$

where we have used $\boldsymbol{j} \times \boldsymbol{B}_0 = \boldsymbol{\nabla} p$ and Ampère's law, and Ω is the gyrofrequency, $v_\perp$ is the particle speed perpendicular to the magnetic field, p is the plasma pressure, $\boldsymbol{B}_0$ is the equilibrium magnetic field, and $\boldsymbol{j}$ is the plasma current density. To lowest order in β and $k_\perp \rho_\mathrm{i}$, the inclusion of compressional magnetic perturbations cancels the pressure-dependent part of the $\boldsymbol{\nabla} B_0$-drift, thus, a lowest-order approximation for the inclusion of compressional magnetic perturbations is to remove the pressure-dependent part of the $\boldsymbol{\nabla} B_0$-drift.[13,18,20,21,42] Using this approximation, Equation (1) becomes

$$v_{\nabla B} = \frac{1}{\Omega}\hat{\boldsymbol{b}} \times \frac{v_\perp^2}{2}\left[\frac{\boldsymbol{\nabla} B}{B} + \frac{4\pi}{B^2}\boldsymbol{\nabla} p\right].$$

The simulation parameters used are as follows. A Miller[43] magnetic equilibrium is used with parameters magnetic shear $\hat{s} = 0.796$, inverse aspect ratio $\epsilon = 0.18$, and safety factor $q_0 = 1.4$, with α being set automatically such that it is consistent with β and the temperature and density gradients of active species. Density and temperature length scales $R_0/L_\mathrm{n} = 2.22$ and $R_0/L_\mathrm{T} = 6.96$, respectively, are used with equal ion and electron temperatures. Gyrokinetic deuterium ions and electrons with real electron mass are considered, and collisions are not included. The mode $k_\mathrm{y}\rho_\mathrm{i} = 0.2$ is considered when performing a scan over electron plasma β. This wavenumber corresponds to toroidal mode number $n = 13$, if we take $B_0 = 2$ T on axis, reference temperature $T_\mathrm{ref} = 2.14$ KeV, reference density $n_\mathrm{ref} = 4.66 \times 10^{19}$ m^{-3}, reference length scale $L_\mathrm{ref} = 1.67$ m, and reference particle mass $m_\mathrm{ref} = 2m_\mathrm{p}$, where m_p is the proton mass.[33] $\beta_\mathrm{e} = 3\%$ is considered when performing a scan over $k_\mathrm{y}\rho_\mathrm{i}$.

The growth rate and real frequency as a function of the electron plasma β and the mode wavenumber $k_\mathrm{y}\rho_\mathrm{i}$ are shown in Figures 1 and 2, respectively. In Figure 1, an ITG to KBM transition is observed, which is in agreement with previous studies,[18,33] and, in addition, a second stability region is observed. Figure 2 is in qualitative agreement with Figure 2 of

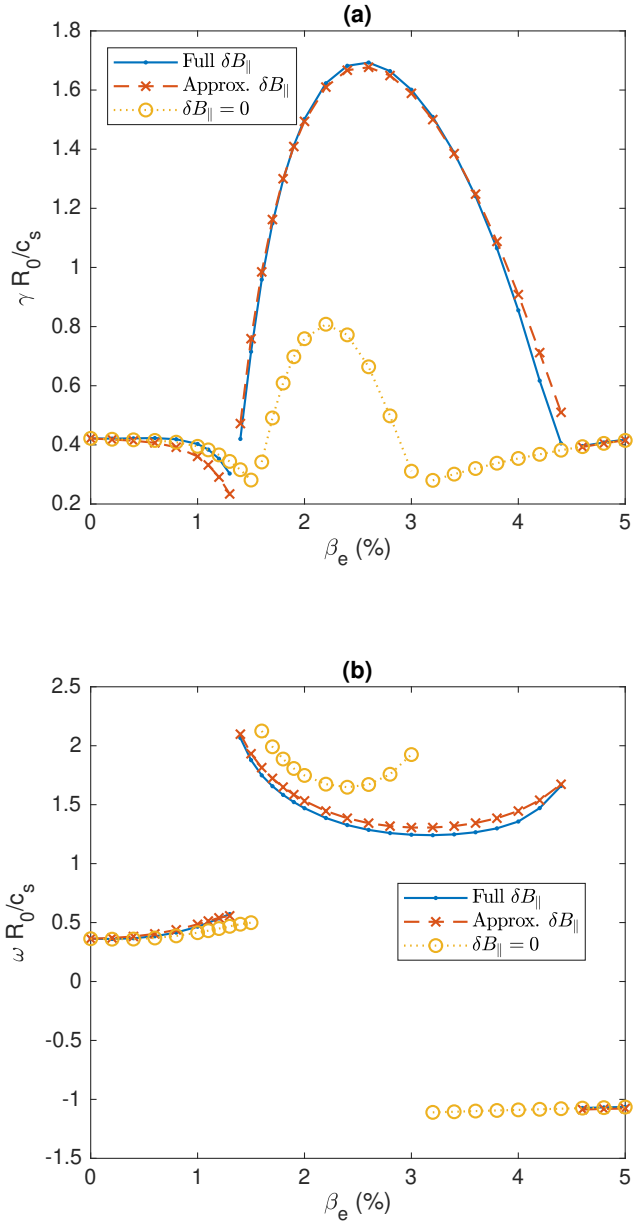

FIG. 1. (a) The normalized growth rate $\gamma R_0/c_\mathrm{s}$ and (b) the normalized real frequency $\omega R_0/c_\mathrm{s}$ as a function of the electron plasma β for the Cyclone Base Case[41] at wavenumber $k_\mathrm{y}\rho_\mathrm{i} = 0.2$ using the local version of the gyrokinetic code GENE[25] with a full $\delta B_\parallel$ model, an approximate $\delta B_\parallel$ model, and $\delta B_\parallel = 0$, where R_0 is the tokamak major radius and c_s is the sound speed.

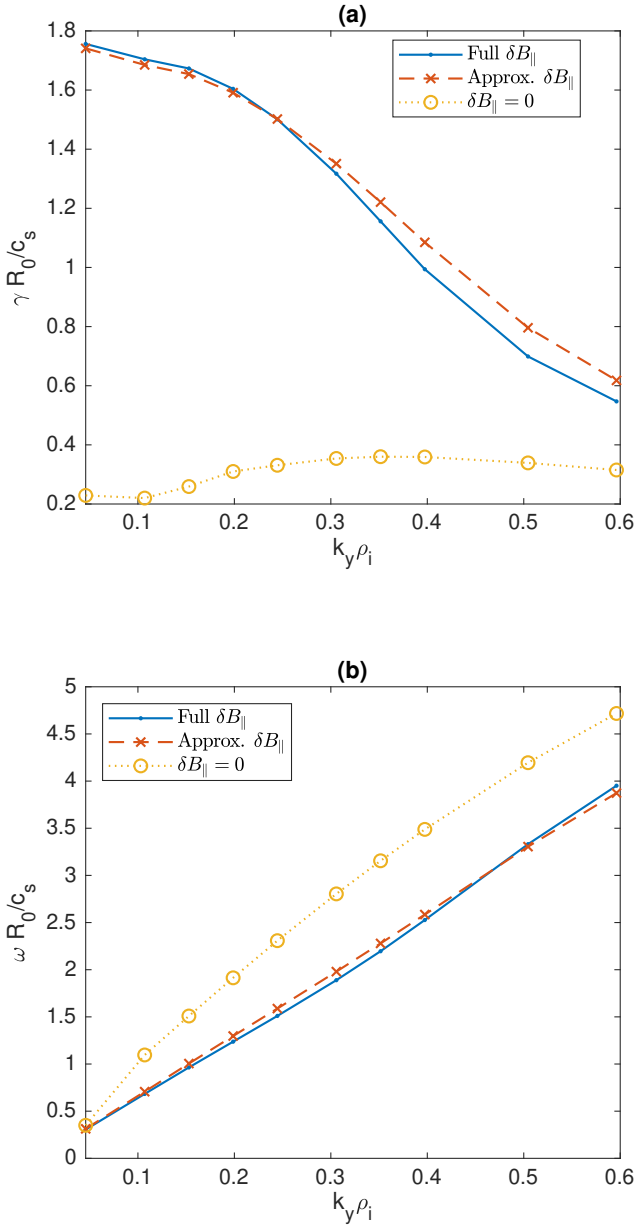

FIG. 2. (a) The normalized growth rate $\gamma R_0/c_\mathrm{s}$ and (b) the normalized real frequency $\omega R_0/c_\mathrm{s}$ as a function of the mode wavenumber $k_\mathrm{y}\rho_\mathrm{i}$ for the Cyclone Base Case[41] at $\beta_\mathrm{e} = 3\%$ using the local version of the gyrokinetic code GENE[25] with a full $\delta B_\parallel$ model, an approximate $\delta B_\parallel$ model, and $\delta B_\parallel = 0$, where R_0 is the tokamak major radius and c_s is the sound speed.

Reference 18. There is good agreement between the full $\delta B_\parallel$ model and the approximate $\delta B_\parallel$ model, whereas a model that completely neglects $\delta B_\parallel$ shows a significant disagreement.

B. Global cross-verification

1. *Electromagnetic gyrokinetic Vlasov equation used in XGC*

The electromagnetic gyrokinetic Vlasov equation[44] used in XGC is

$$
\begin{aligned}
&\frac{\partial f}{\partial t} + \dot{\boldsymbol{R}} \cdot \boldsymbol{\nabla} f + \dot{u}_\parallel \frac{\partial f}{\partial u_\parallel} = 0, \\
&\dot{\boldsymbol{R}} = \frac{D}{B_0}\left(\frac{\boldsymbol{B}^*}{m}\frac{\partial H}{\partial u_\parallel} + \frac{\boldsymbol{F}\times\boldsymbol{B}_0}{B_0}\right), \\
&\dot{u}_\parallel = \frac{q}{m}\left(D\frac{\boldsymbol{B}^*}{B_0}\cdot\boldsymbol{F} - \frac{\partial A_\parallel^{\mathrm{s}}}{\partial t}\right), \\
&u_\parallel = v_\parallel + \frac{q}{m}\left\langle A_\parallel^{\mathrm{h}}\right\rangle, \\
&\frac{\partial A_\parallel^{\mathrm{s}}}{\partial t} = -\hat{\boldsymbol{b}}\cdot\boldsymbol{\nabla}\phi, \\
&D = \frac{B_0}{B_\parallel^*} = \left[1 + \left(\frac{m u_\parallel}{q B_0} + \frac{\left\langle A_\parallel^{\mathrm{s}}\right\rangle}{B_0}\right)\hat{\boldsymbol{b}}\cdot\boldsymbol{\nabla}\times\hat{\boldsymbol{b}}\right]^{-1}, \\
&\boldsymbol{B}^* = \boldsymbol{\nabla}\times\boldsymbol{A}^*, \\
&\boldsymbol{A}^* = \boldsymbol{A}_0 + \left(\frac{m}{q}u_\parallel + \left\langle A_\parallel^{\mathrm{s}}\right\rangle\right)\hat{\boldsymbol{b}}, \\
&H = \frac{m}{2}u_\parallel^2 + \mu B_0 + q\left(\langle\phi\rangle - u_\parallel\left\langle A_\parallel^{\mathrm{h}}\right\rangle\right) + \frac{q^2}{2m}\left\langle A_\parallel^{\mathrm{h}}\right\rangle^2, \\
&\boldsymbol{F} = -\frac{1}{q}\boldsymbol{\nabla}H = -\frac{\mu}{q}\boldsymbol{\nabla}B_0 - \boldsymbol{\nabla}\langle\phi\rangle + u_\parallel\boldsymbol{\nabla}\left\langle A_\parallel^{\mathrm{h}}\right\rangle - \frac{q}{m}\left\langle A_\parallel^{\mathrm{h}}\right\rangle\boldsymbol{\nabla}\left\langle A_\parallel^{\mathrm{h}}\right\rangle, \\
&B_\parallel^* = \hat{\boldsymbol{b}}\cdot\boldsymbol{B}^*,
\end{aligned}
\tag{2}
\tag{3}
$$

where $f(Z,t)$ is the gyrocenter distribution function, $Z = (\boldsymbol{R}, u_\parallel, \mu)$, $\boldsymbol{R}$ is the gyrocenter position, $v_\parallel$ is the parallel velocity, q is the particle charge, m is the particle mass, angle brackets denote the gyroaverage, $A_\parallel^{\mathrm{h}}$ is the Hamiltonian component of $A_\parallel$, $A_\parallel$ is the parallel component of the perturbed magnetic potential, μ is the magnetic moment, t is time, $A_\parallel^{\mathrm{s}}$ is the symplectic component of $A_\parallel$, and ϕ is the perturbed electrostatic potential.

Once again, to lowest order in β and $k_\perp\rho_{\mathrm{i}}$, the inclusion of compressional magnetic perturbations cancels the pressure-dependent part of the $\boldsymbol{\nabla}B_0$-drift, thus, a lowest-order ap-

proximation for the inclusion of compressional magnetic perturbations is to remove the pressure-dependent part of the $\boldsymbol{\nabla} B_0$-drift.[13,18,20,21,42] Using this approximation, Equations (2) and (3) become

$$\dot{\boldsymbol{R}} = \frac{D}{B_0}\left(\frac{\boldsymbol{B}^*}{m}\frac{\partial H}{\partial u_\parallel} + \frac{\boldsymbol{F}\times\boldsymbol{B}_0}{B_0} + \frac{\mu}{q}B_0\boldsymbol{\nabla}\times\hat{\boldsymbol{b}}\right),$$
$$\boldsymbol{F} = -\frac{1}{q}\boldsymbol{\nabla}H = -\boldsymbol{\nabla}\langle\phi\rangle + u_\parallel\boldsymbol{\nabla}\left\langle A_\parallel^{\mathrm{h}}\right\rangle - \frac{q}{m}\left\langle A_\parallel^{\mathrm{h}}\right\rangle\boldsymbol{\nabla}\left\langle A_\parallel^{\mathrm{h}}\right\rangle.$$

The field equations[44] remain unmodified and, for completeness, we include them here. The Poisson equation in the long-wavelength limit is

$$-\nabla\cdot\frac{m_{\mathrm{i}}n_{\mathrm{i}0}}{B_0^2}\nabla_\perp\phi = q_{\mathrm{i}}\langle n_{\mathrm{i}}\rangle + q_{\mathrm{e}}n_{\mathrm{e}},$$

where the subscripts "i" and "e" denote ions and electrons, respectively, $n_{\mathrm{i}0}$ is the background ion density, and n is the density. The Ampère equation is

$$-\nabla\cdot\nabla_\perp A_\parallel^{\mathrm{h}} + A_\parallel^{\mathrm{h}}\sum_{s=\mathrm{i,e}}\frac{\mu_0 n_0 q_s^2}{m_s} = \mu_0\left(\langle j_{\parallel\mathrm{i}}\rangle + j_{\parallel\mathrm{e}}\right) + \nabla\cdot\nabla_\perp A_\parallel^{\mathrm{s}},$$

where μ_0 is the vacuum magnetic permeability, and $j_\parallel$ is the parallel current density, which is given by the first $u_\parallel$ moment of the distribution function.

2. Cross-verification

Cross-verification has been performed using the global gyrokinetic code XGC and the global versions of the gyrokinetic codes GEM[45] and GENE, where all three codes used the same $\delta B_\parallel$ model. Cross-verification between XGC, GEM, and GENE has previously been performed for ITGs, CTEMs, and KBMs.[16,32] We emphasize that GEM and GENE are only used here for cross-verification purposes, and only XGC is used for physics studies.

The plasma model that is used is based on that in Reference 32, which was designed to save computing resources when performing physics parameter scans using numerous global gyrokinetic simulations. We refer to this case as the Economical Cyclone Base Case (ECBC), as the ratio of the ion gyroradius to tokamak minor radius ρ^* is approximately 1/50, compared to approximately 1/180 for the CBC. We define the magnetic equilibrium as $R_0 = 2.8$ m, $a = 1.0$ m, $\kappa = 1.0$, $\delta = 0.0$, $B_0 = 0.2364$ on axis, safety factor (Figure 3)

$$q = 0.8241 + 0.9220\psi_{\mathrm{N}} + 1.390\psi_{\mathrm{N}}^2,$$

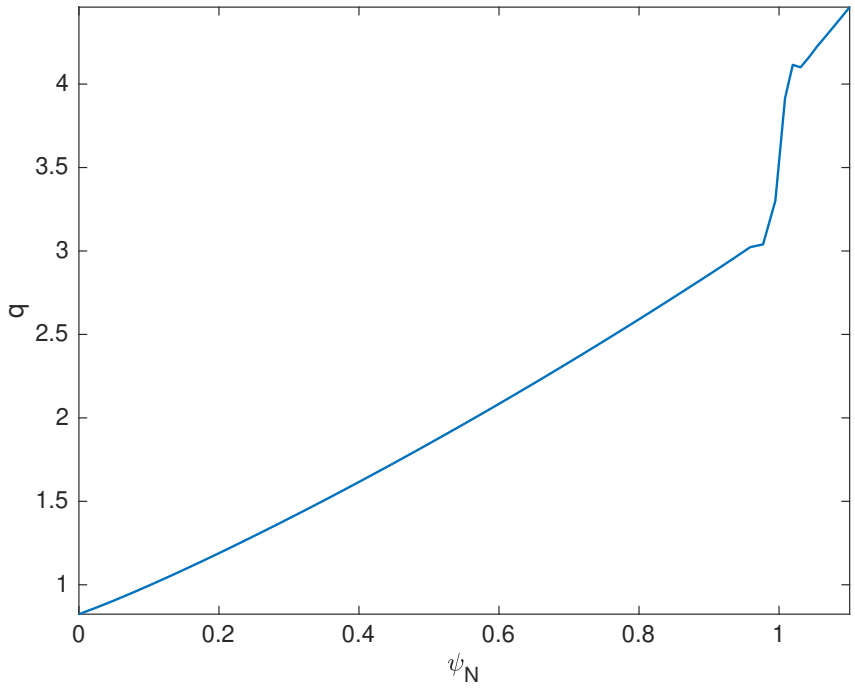

FIG. 3. Safety factor q as a function of the normalized poloidal magnetic flux ψ_N for the case described in Subsection III B.

and pressure

$$P = 2n_e T,$$

where n_e is the electron density and T is the ion and electron temperature. We define the $\beta_e(\psi_N = 0.5) = \mu_0 n_e(\psi_N = 0.5)T_e(\psi_N = 0.5)/B_0^2 = 0.5\%$ electron density and temperature

profiles (Figure 4) as

$$n_{\rm e} = \frac{1}{2}(n_{\rm e1} + n_{\rm e2}) + \frac{1}{2}(n_{\rm e1} - n_{\rm e2}) \tanh\left[2\frac{(n_{\rm e3} - \psi_{\rm N})}{n_{\rm e4}}\right],$$

$$n_{\rm e1} = 7.483 \times 10^{17}\ {\rm m}^{-3},$$

$$n_{\rm e2} = 5.483 \times 10^{17}\ {\rm m}^{-3},$$

$$n_{\rm e3} = 0.5,$$

$$n_{\rm e4} = 0.5,$$

$$T = \frac{1}{2}(T_1 + T_2) + \frac{1}{2}(T_1 - T_2) \tanh\left[2\frac{(T_3 - \psi_{\rm N})}{T_4}\right],$$

$$T_1 = 3.14\ {\rm keV},$$

$$T_2 = 1.14\ {\rm keV},$$

$$T_3 = 0.5,$$

$$T_4 = 0.5,$$

respectively. The density profiles for other $\beta_{\rm e}$ values were obtained by scaling $n_{\rm e}$, and these were then used when reconstructing the magnetic equilibria. We consider gyrokinetic hydrogen ions and drift-kinetic electrons with real electron mass. The toroidal mode number considered is $n = 6$, which corresponds to $k_\theta \rho_{\rm i} = 0.36$.

The simulation parameters used by XGC are as follows. All toroidal mode numbers were filtered out except $n = 6$, and only poloidal modes in the range $|m - nq| \leq 5$ were kept. There was no change in the results when using the alternative choice of only keeping poloidal modes in the range $|m/q - n| \leq 3$. This alternative choice may assist the formation of truly global modes in high-q regions by increasing the range of poloidal modes that are included. An ion time step $\Delta t = 2.5 \times 10^{-2} v_{\rm A} = 1.0 \times 10^{-8}$ s was used, where $v_{\rm A}$ is the Alfvén time for the $\beta_{\rm e} = 0.5\%$ case at $\psi_{\rm N} = 0.95$, and electrons were subcycled[6] at a quarter of this time step, with the field solver being executed at every ion time step. An unstructured triangular mesh[46] with a spacing $\Delta l = 0.5\rho_{\rm i}$ was used on each poloidal plane, where $\rho_{\rm i}$ is the thermal ion gyroradius. Mesh nodes that are approximately field-aligned allow the use of a relatively low toroidal resolution. The simulation domain was in the range $0 \leq \psi_{\rm N} \leq 1.1$, and the perturbed fields were set to zero for $\psi_{\rm N} < 0.1$ and $\psi_{\rm N} > 1$. A one sixth torus was used in the toroidal direction (a toroidal wedge model), with eight grid points in the toroidal direction within this toroidal wedge. The maximum toroidal mode number that is supported by the

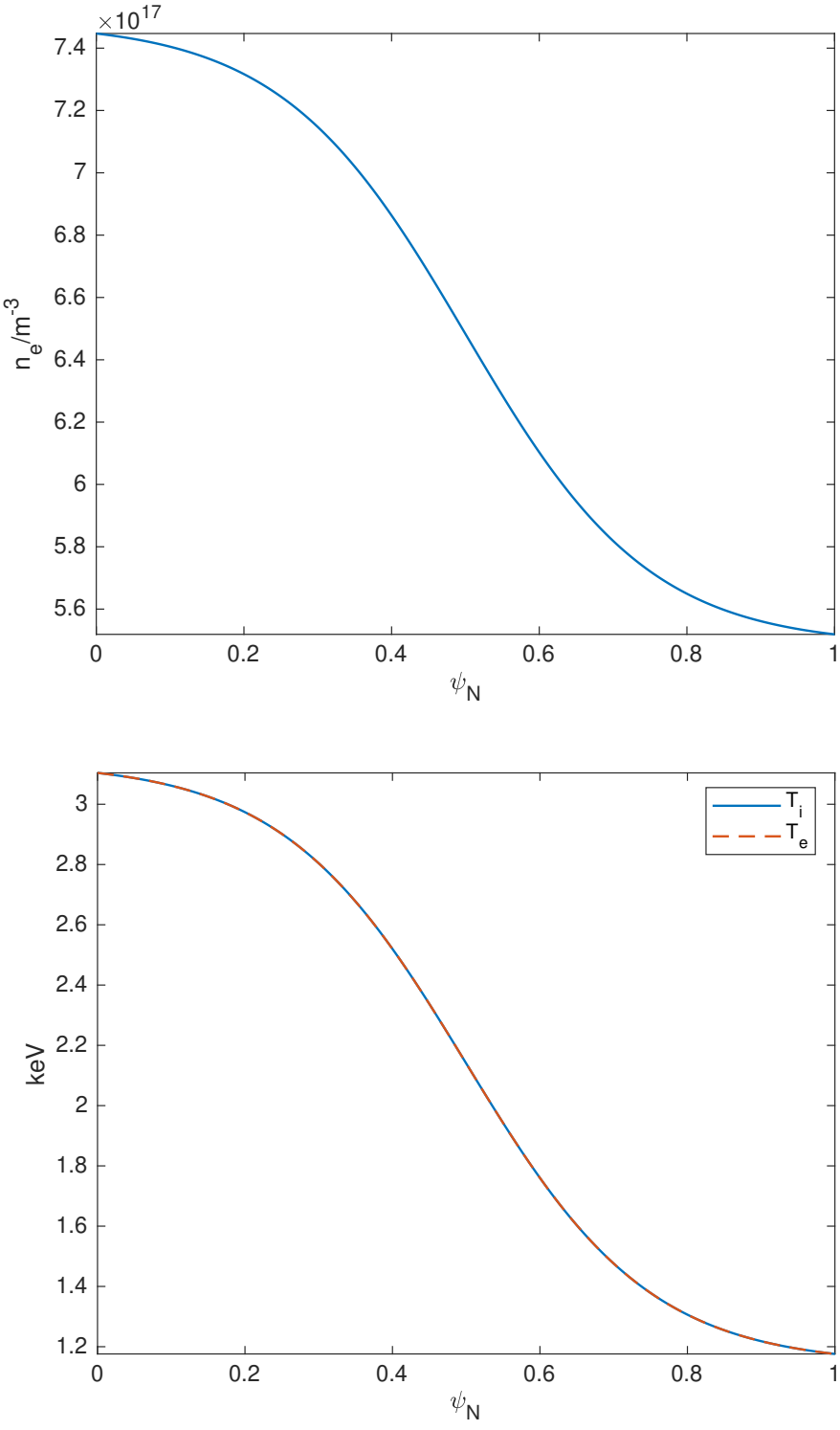

FIG. 4. Electron density n_{e} (top) and ion and electron temperature $T_{\mathrm{i,e}}$ (bottom) as a function of the normalized poloidal magnetic flux ψ_{N} for the $\beta_{\mathrm{e}} = 0.5\%$ case described in Section III.

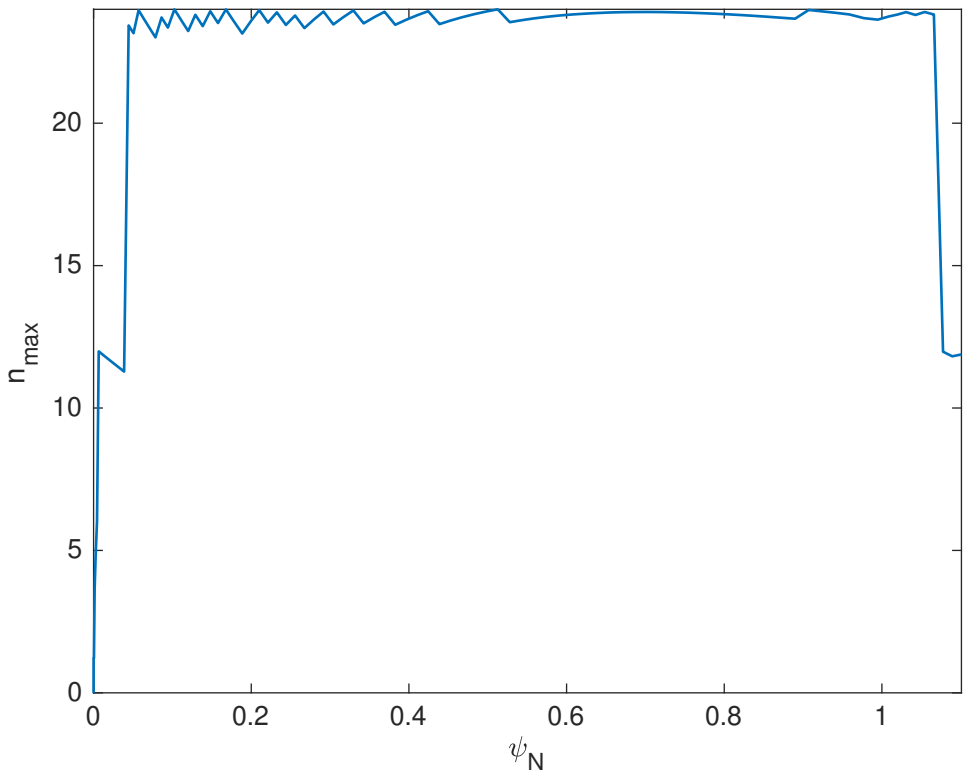

FIG. 5. The maximum toroidal mode number $n_{\max}$ that is supported by the mesh as a function of the normalized poloidal magnetic flux ψ_{N} for the $\beta_{\mathrm{e}} = 0.5\%$ case described in Section III.

mesh is

$$n_{\max} = \frac{m_{\max}}{q},$$

where $m_{\max}$ is the maximum poloidal mode number that is supported by the mesh. This is shown in Figure 5 for $\beta_{\mathrm{e}} = 0.5\%$, where $n_{\max}$ is approximately equal to 24 within the region of non-zero perturbed fields. Fields were solved in the long-wavelength limit.[16,32] 100 numerical markers per mesh vertex were used.

The growth rate and real frequency as a function of β_{e} for the three codes involved in this global cross-verification are shown in Figure 6. At low β_{e}, modes propagating in the ion diamagnetic direction are present, and these modes are stabilized as β_{e} is increased. Thus, we identify these modes as ITGs. The radial location of the mode is compatible with an analytic estimate[47] for the ITG growth rate, as shown in Figure 7 for XGC.

At approximately $\beta_{\mathrm{e}} = 1\%$, the mode transitions from an ITG to a KBM. The transition is characterized by a large, discontinuous increase in real frequency. As β_{e} is increased

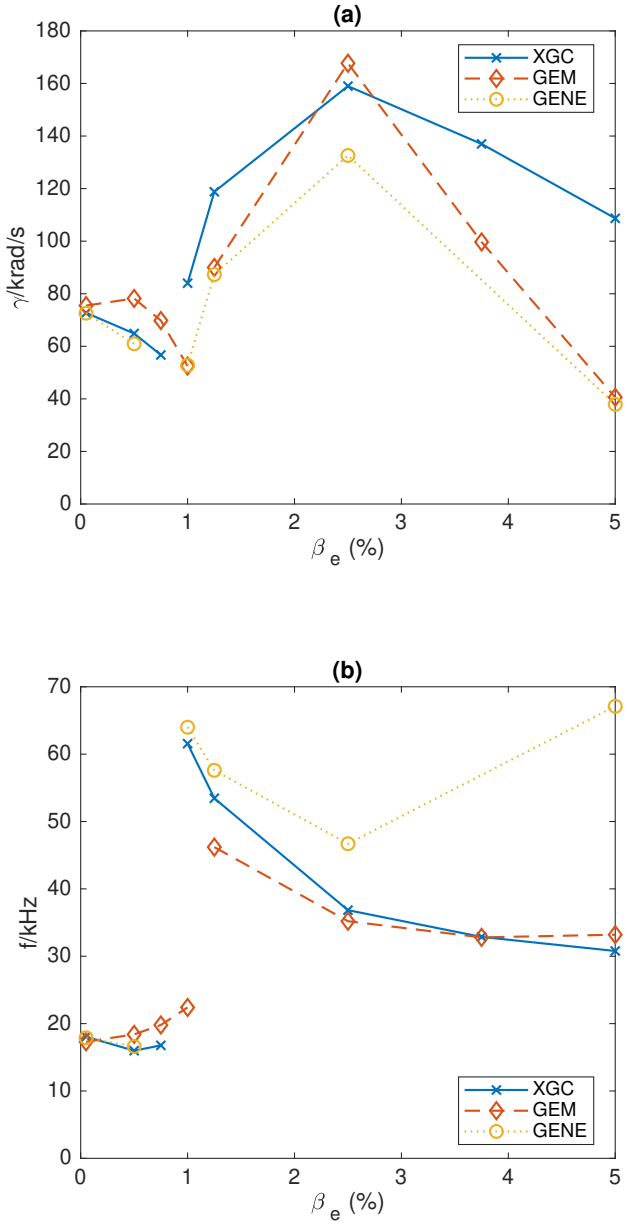

FIG. 6. (a) Growth rate γ and (b) real frequency f as a function of electron plasma β for the global gyrokinetic codes XGC and the global versions of the gyrokinetic codes GEM and GENE with the same approximate $\delta B_{||}$ model for the case described in Section III. Positive frequency corresponds to the ion diamagnetic direction, and the units correspond to the fields varying as $e^{i\omega t}$, where ω is the complex angular frequency.

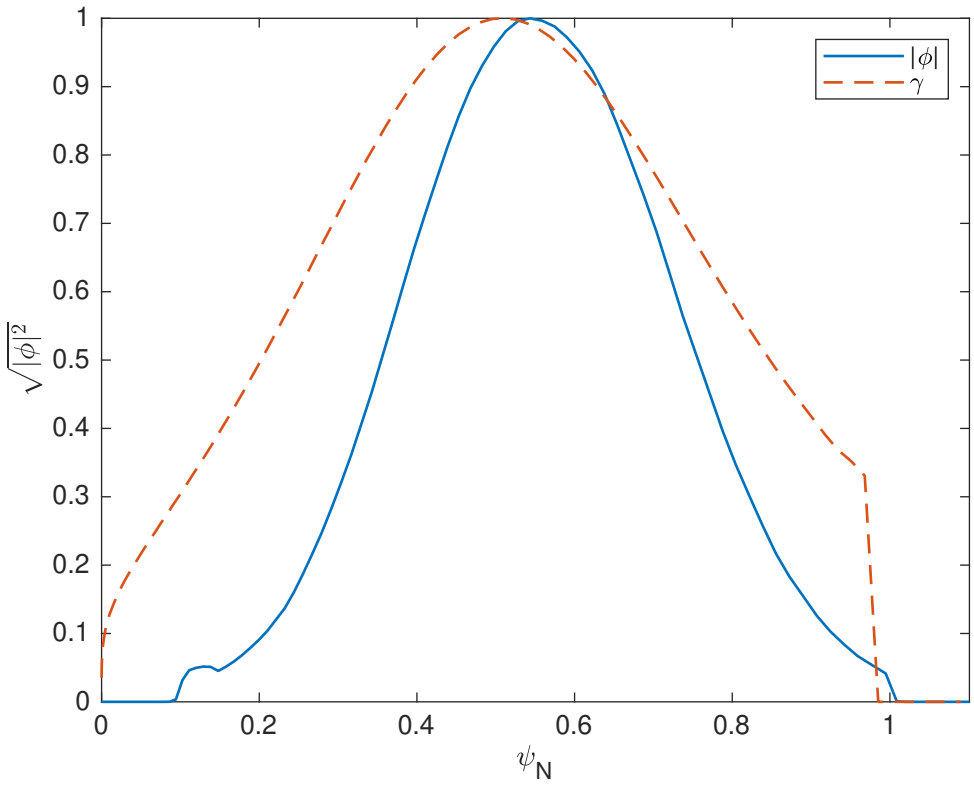

FIG. 7. The mode structure for the absolute value of the electrostatic potential $|\phi|$ as a function of the normalized poloidal magnetic flux ψ_N is compatible with the an analytic estimate[47] for the growth rate γ of the ion temperature gradient mode at $\beta_e = 0.05\%$ for XGC for the case described in Section III, where arbitrary units are used for $|\phi|$ and γ.

further, there is destabilization and then stabilization of the KBM. The radial location of the mode is compatible with the KBM drive, which is the normalized pressure gradient $\alpha = -2\mu_0 q^2 R_0 \nabla P / B_0^2$, as shown in Figure 8 for XGC.

There is reasonably good agreement between the three global gyrokinetic codes XGC, GEM, and GENE. At $\beta_e = 5\%$, which is five times the critical β_e, there is greater variation between the three codes, but this is unsurprising this far from the transition. At higher β_e, it is likely that the significant Shafranov shift and flux-surface compression requires higher resolution in order to obtain better agreement, especially given that one pair of codes (GEM and GENE) agree for growth rate, whereas a different pair of codes (XGC and GEM) agree for real frequency.

The radial location of the modes is shown as a function of β_e in Figure 9 for XGC.

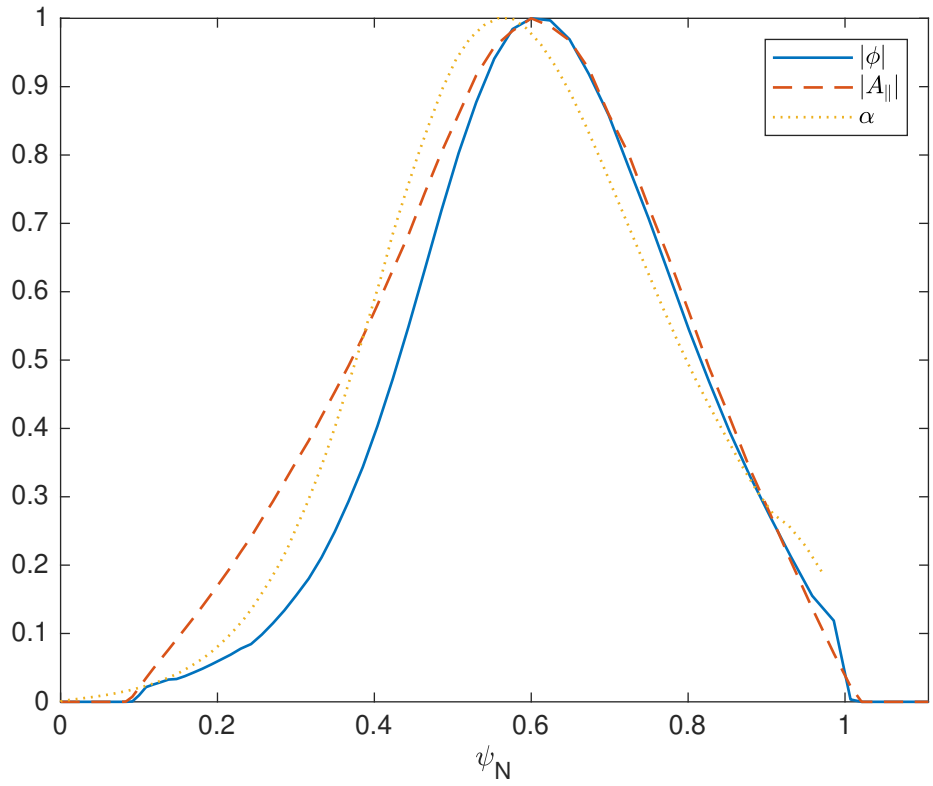

FIG. 8. The mode structure for the absolute values of the electrostatic potential $|\phi|$ and the parallel magnetic potential $|A_\parallel|$ as a function of the normalized poloidal magnetic flux ψ_N is compatible with the kinetic ballooning mode drive, which is the normalized pressure gradient $\alpha = -2\mu_0 q^2 R_0 \nabla P / B_0^2$, at $\beta_e = 2.5\%$ for XGC for the case described in Section III, where arbitrary units are used for $|\phi|$, $|A_\parallel|$, and α.

KBMs peak further outward radially than ITGs because of these two different modes having different instability drives (Table I and Figures 7 & 8).

Example ITG and KBM mode structures from XGC are shown in Figure 10. The Shafranov shift is significantly larger for the KBM cases than for the ITG cases. For example, for the $\beta_e = 0.05\%$ and $\beta_e = 2.5\%$ cases, the major radius of the magnetic axis is $R_{axis} = 2.88$ m and $R_{axis} = 3.11$ m, respectively. The $\beta_e = 2.5\%$ case was also run with 10 times as many markers with XGC, and the differences in the growth rate and real frequency remained within 5%.

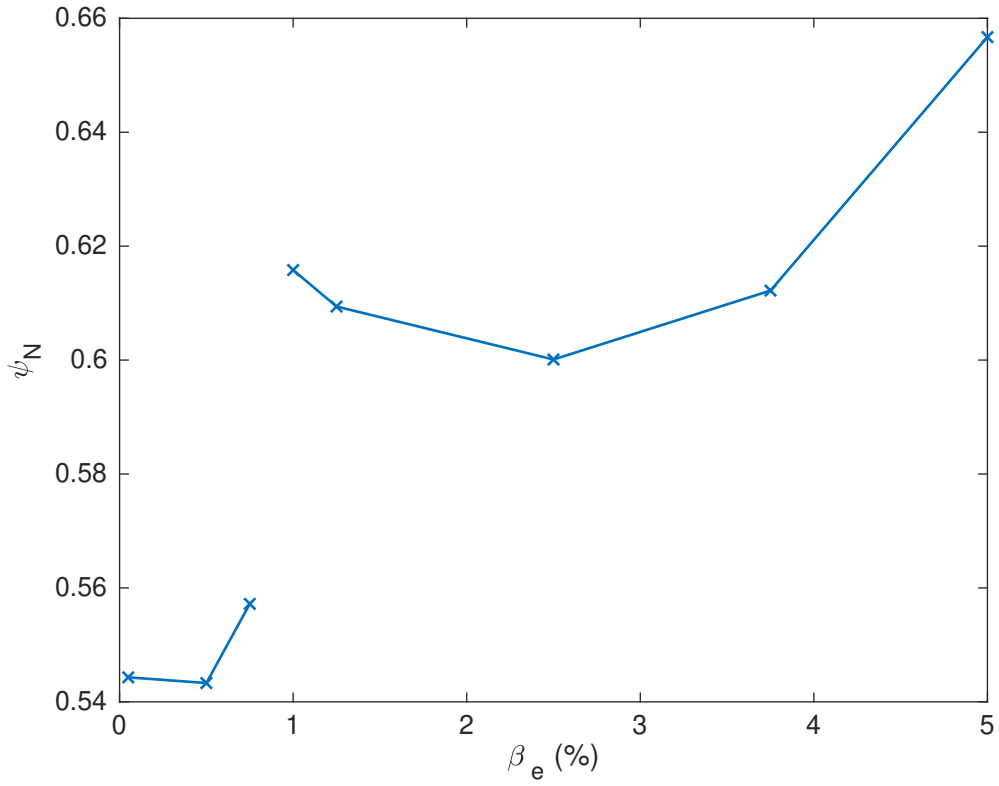

FIG. 9. Mode radial location in terms of the normalized poloidal magnetic flux ψ_N as a function of the electron plasma β for XGC for the case described in Section III.

IV. SHAPING STUDY

Following the cross-verification of the simplified compressional mode formula, XGC has been used to study on shaping effects at the NSTX aspect ratio. We emphasize that GEM and GENE were only used for verification and cross-verification, while XGC was used for physics studies.

The magnetic geometries that were used in this study are based on NSTX discharge 132588[8,48,49] at 650 ms. This discharge is a highly shaped, high-performance enhanced pedestal (EP) H-mode discharge. Three magnetic geometries were considered, as described in Table II and shown in Figure 11. All of the geometries use the same aspect ratio as NSTX discharge 132588. The first geometry has a circular cross-section. The second geometry has a highly elongated cross-section, with an elongation identical to that of NSTX discharge number 132588. The third geometry has a highly elongated and highly triangular

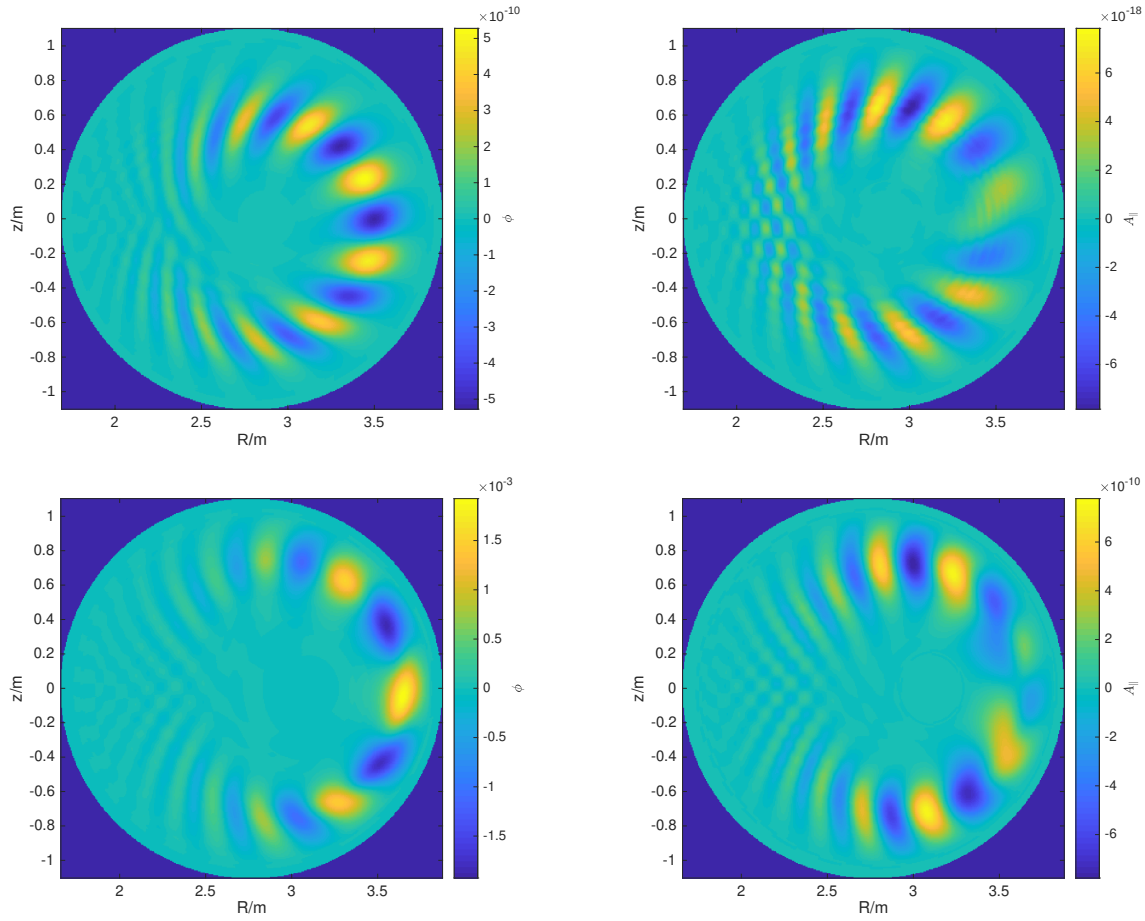

FIG. 10. Mode structures for the perturbed electrostatic ϕ (first column) and parallel magnetic $A_{\|}$ (second column) potentials in the (R, z) plane for the ITG at $\beta_e = 0.05\%$ (top row) and the KBM at $\beta_e = 2.5\%$ (bottom row) from the global gyrokinetic code XGC for the case described in Section III.

cross-section, with elongation and triangularity identical to that of NSTX discharge 132588. NSTX discharge 132588 includes up-down asymmetry, especially in the edge region, due to the divertor separatrix, however, up-down asymmetry is not included in any of the geometries considered here. The magnetic field strength and safety factor profile (Figure 12) are identical to that of NSTX discharge 132588 for all three geometries up to $\psi_N = 0.99$.

We define the $\beta_e(\psi_N = 0.5)$=15% electron density and temperature profiles (Figure 13)

Geometry	Aspect ratio A	Elongation κ	Triangularity δ
Circular	1.4	1.0	0.0
Elongated	1.4	2.2	0.0
Elongated, triangular	1.4	2.2	0.55

TABLE II. The shaping parameters used for the magnetic geometries that were considered in the shaping study described in Section IV.

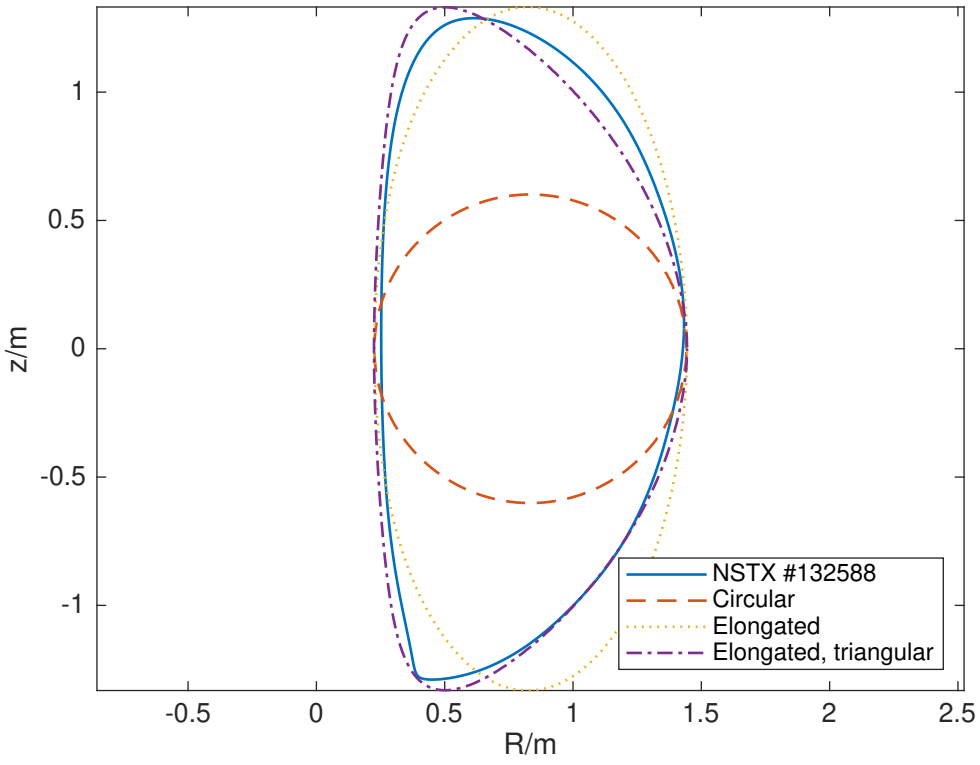

FIG. 11. The shapes of NSTX discharge 132588 and the magnetic geometries considered in the shaping study described in Section IV.

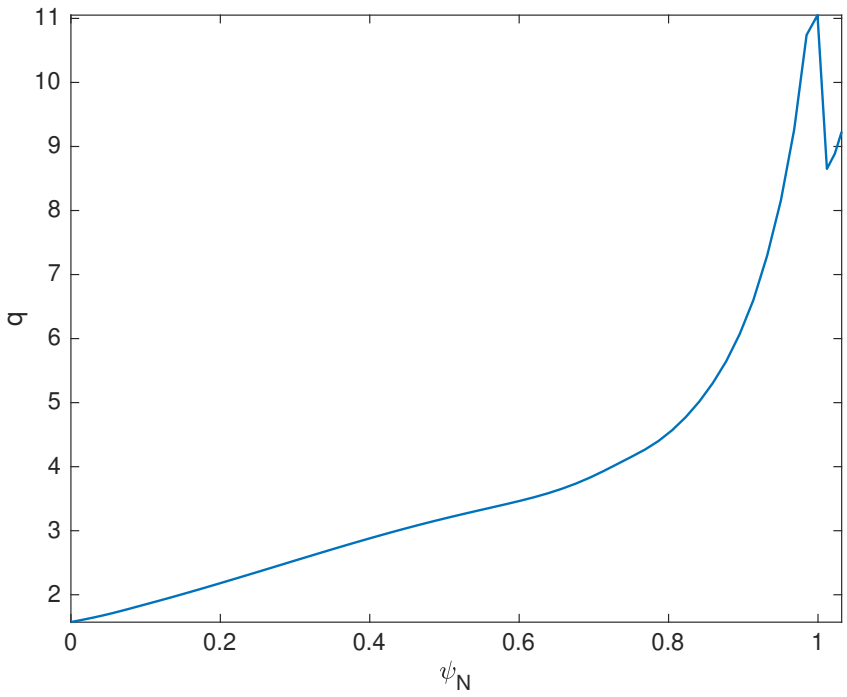

FIG. 12. Safety factor q as a function of the normalized poloidal magnetic flux ψ_N for the case described in Section IV. The magnetic field strength on axis is $B_0 = 0.4370$.

as

$$n_e = \frac{1}{2}(n_{e1} + n_{e2}) + \frac{1}{2}(n_{e1} - n_{e2}) \tanh\left[2\frac{(n_{e3} - \psi_N)}{n_{e4}}\right],$$

$$n_{e1} = 7.6 \times 10^{19}\ \mathrm{m}^{-3},$$

$$n_{e2} = 5.6 \times 10^{19}\ \mathrm{m}^{-3},$$

$$n_{e3} = 0.5,$$

$$n_{e4} = 0.5,$$

$$T = \frac{1}{2}(T_1 + T_2) + \frac{1}{2}(T_1 - T_2) \tanh\left[2\frac{(T_3 - \psi_N)}{T_4}\right],$$

$$T_1 = 3.179\ \mathrm{keV},$$

$$T_2 = 1.179\ \mathrm{keV},$$

$$T_3 = 0.5,$$

$$T_4 = 0.5,$$

respectively. For comparison, we show the β_e profile for NSTX discharge 132588 in Figure

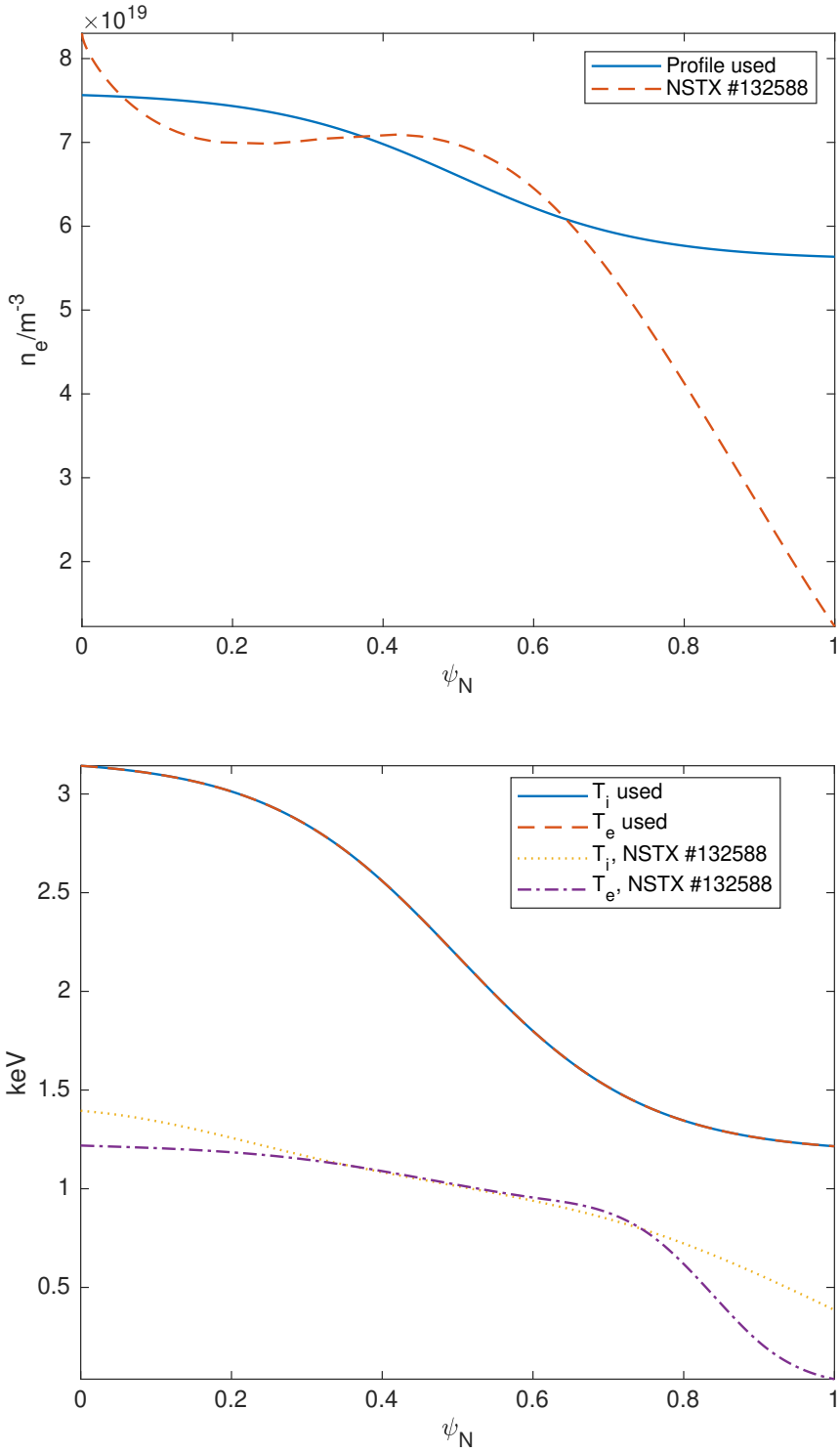

FIG. 13. Electron density n_e (top) and ion and electron temperature $T_{i,e}$ (bottom) as a function of the normalized poloidal magnetic flux ψ_N for the case described in Section IV. For reference, we include the electron density and temperature profiles for NSTX discharge 132588.

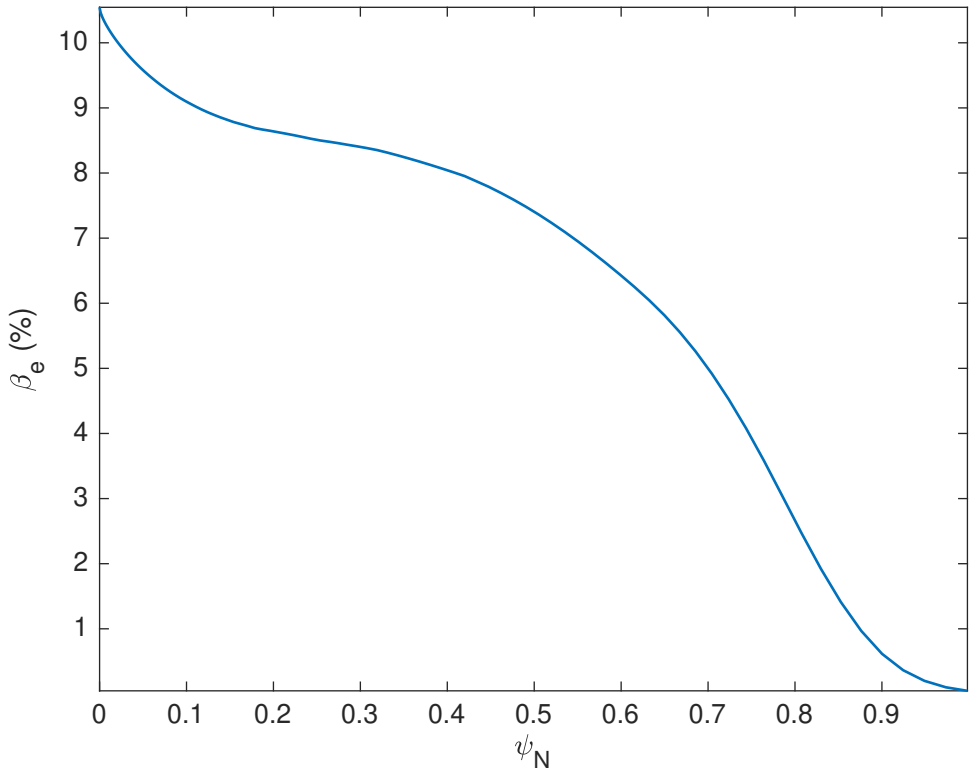

FIG. 14. The electron plasma β as a function of the normalized poloidal magnetic flux ψ_N for NSTX discharge 132588.

14. The plasma profiles used in this study are very different from those of NSTX discharge 132588 and, as such, this study is purely an investigation of the impact of plasma shaping on generic stability characteristics. Shaping effects in the strong gradients of the pedestal could be very different. The density profiles for other β_e values were obtained by scaling n_e, and these were then used when reconstructing the magnetic equilibria. We consider gyrokinetic hydrogen ions and drift-kinetic electrons with real electron mass, whereas NSTX discharge 132588 used deuterium ions (not hydrogen), and also had carbon impurities present, which are not simulated here, although this capability exists in XGC[50] and will be used in the future. Coulomb collisions are not included. The toroidal mode number considered in this study is $n = 20$, which corresponds to $k_\theta \rho_i = 0.95$, where microinstability is generally strong.

The simulation parameters that were used were identical to those in Section III B 2, apart from the following. All toroidal mode numbers were filtered out except $n = 20$. $\Delta t = 1.4 \times 10^{-2} v_A = 1.4 \times 10^{-8}$ s was used, where v_A is defined for the $\beta_e = 15\%$ case at

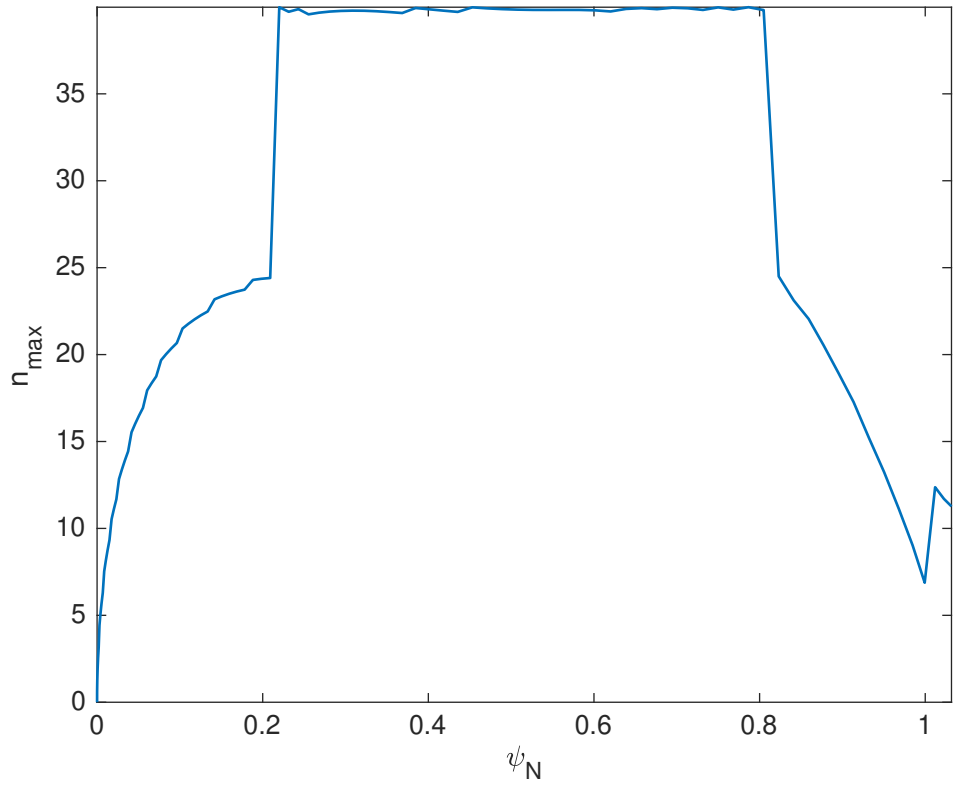

FIG. 15. The maximum toroidal mode number $n_{\max}$ that is supported by the mesh as a function of the normalized poloidal magnetic flux $\psi_{\rm N}$ for the $n = 20$ elongated, triangular geometry case at $\beta_{\rm e} = 15\%$ that is described in Section IV.

$\psi_{\rm N} = 0.95$. A one twentieth torus was used. The maximum toroidal mode number that is supported by the mesh for the elongated, triangular geometry case at $\beta_{\rm e} = 15\%$ is shown in Figure 15.

The growth rate and real frequency as a function of electron plasma β are shown in Figure 16. We first discuss the results for which approximate $\delta B_{\parallel}$ effects were included.

For all three geometries at $\beta_{\rm e} = 1\%$, a collisionless trapped electron mode (CTEM) is present. The mode is characterized by ballooning parity and a frequency that is in the electron diamagnetic direction.

For the circular geometry case, as $\beta_{\rm e}$ is increased, there is a CTEM to CMTM transition. The transition is characterized by an increase in growth rate, a relatively large increase in the magnitude of the frequency, which remains in the electron diamagnetic direction, and a change from ballooning to tearing parity. CMTMs are present up to $\beta_{\rm e} = 20\%$. Example

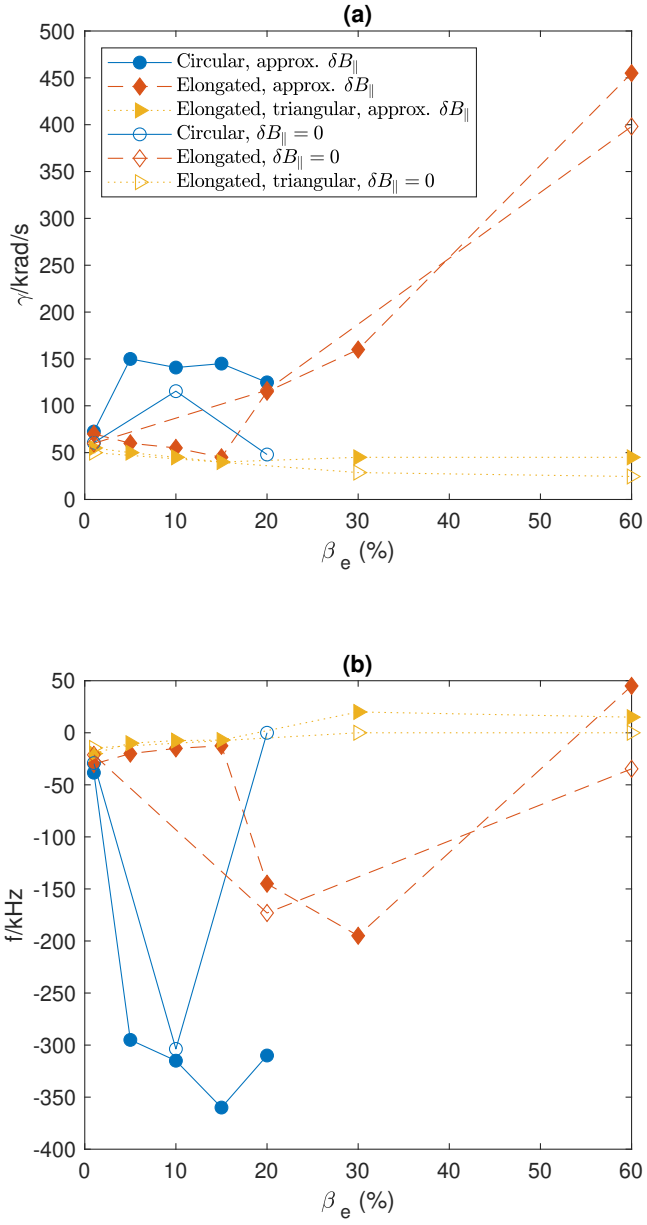

FIG. 16. (a) Growth rate γ and (b) real frequency f as a function of electron plasma β for the shaping study described in Section IV. Positive frequency corresponds to the ion diamagnetic direction, and the units correspond to the fields varying as $e^{i\omega t}$, where ω is the complex angular frequency.

CMTM mode structures for the circular geometry case are shown in Figures 17 and 18, where some of the rational surfaces in the vicinity of the mode are indicated, and the confirmation of tearing parity corresponding to this example is shown in Figure 19. One limitation of the present study is that a convergence study to higher radial resolution may be required in order to ensure a more accurate represention of the full spectrum of nonlocal CMTM behavior that is supported by the configuration (i.e., kinetic electron dynamics across nearby high mode-number rational surfaces), in addition to obtaining better agreement with analytic estimates for growth rate and frequency. The circular geometry case has also been run for $\beta_e = 30\%$ and $\beta_e = 60\%$, where $\beta_e = 30\%$ corresponds to approximately ten times the critical β_e. However, the simulations became numerically unstable before growth rates could be reasonably determined because of extremely fast and unsteady initial growth that is similar ($\beta_e = 30\%$) or exceeds ($\beta_e = 60\%$) the ion gyrofrequency at the outboard midplane. The validity of gyrokinetic equations is limited to the physics of frequencies lower than the gyrofrequency.[51] For both the $\beta_e = 30\%$ and $\beta_e = 60\%$ cases, the mode parity indicated that the modes that were numerically unstable were KBMs. A total-f simulation that has significantly reduced time step and includes self-consistent background profile relaxation may by necessary in order to handle these modes. This work will be reported elsewhere.

For the elongated geometry case, the CTEM branch continues up to $\beta_e = 15\%$, and the CTEM to CMTM transition occurs at $\beta_e = 20\%$. The CMTM branch continues up to $\beta_e = 30\%$. At $\beta_e = 60\%$, there is CMTM to KBM transition. The alternative possibility of a CMTM to ITG transition may be ruled out as the transition occurs at a relatively high value of β_e, for which ITGs should be stabilized and KBMs destabilized. In other words, elongation tends to suppress CMTMs. Example CTEM mode structures for the elongated geometry case are shown in Figure 20.

For the elongated, triangular geometry case, the CTEM branch also continues up to $\beta_e = 15\%$, however, instead of a CTEM to CMTM transition at $\beta_e = 15\%$, there is a CTEM to KBM transition, and CMTMs are not observed. The transition is characterized by the real frequency changing from being in the electron diamagnetic direction to being in the ion diamagnetic direction. The alternative possibility of a CTEM to ITG transition may be ruled out as the transition occurs at a relatively high value of β_e, for which ITGs should be stabilized and KBMs destabilized. Compared to the circular and elongated geometry cases, the elongated, triangular geometry case exhibits only relatively small changes in the

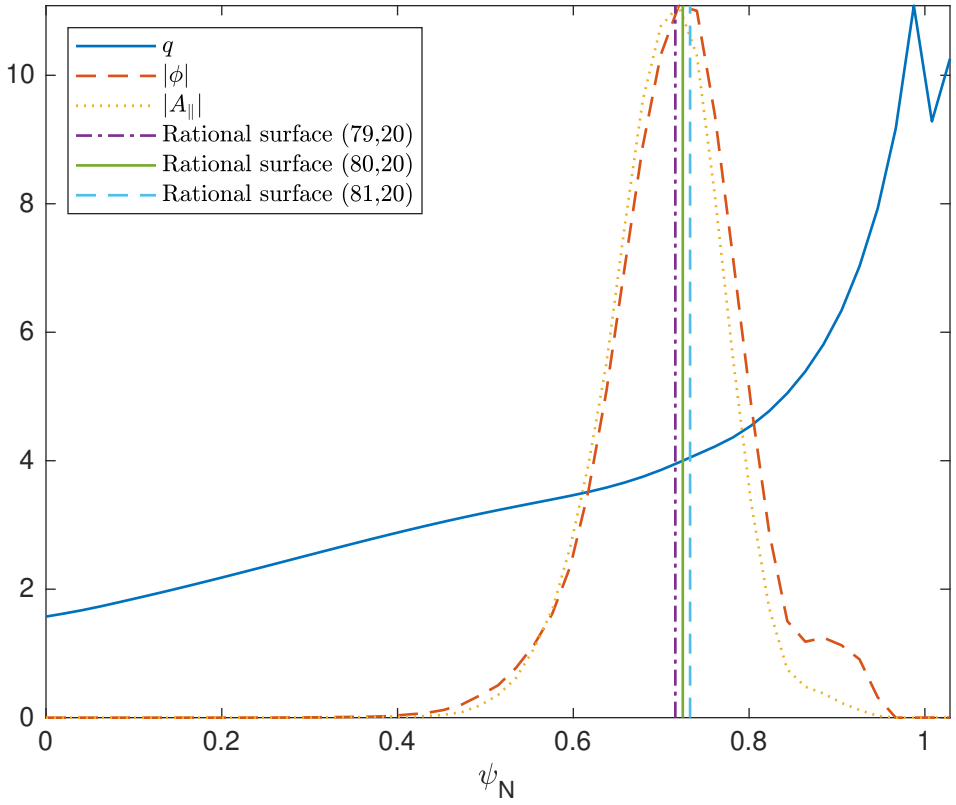

FIG. 17. The safety factor q and the absolute values of the electrostatic potential $|\phi|$ and the parallel magnetic potential $|A_{\|}|$ as a function of the normalized poloidal magnetic flux ψ_{N} for the CMTM at $\beta_{\mathrm{e}} = 10\%$ for the $n = 20$ circular geometry case described in Section IV, where some of the rational surfaces is indicated.

growth rate and real frequency when transitioning between different modes through varying β_{e}. At the NSTX aspect ratio that was used in this study, the linear growth rates of CMTMs and KBMs are all significantly reduced for the elongated and elongated, triangular geometry cases compared to the circular geometry case. CMTMs are even suppressed in the elongated, triangular geometry case compared to the elongated case, leaving the CTEMs as the dominant modes around the experimental or lower β_{e} ranges. The physical reason for the relatively small changes in growth rate and suppression of CMTMs may be that the addition of triangularity causes significant variation of the field line pitch, which stabilizes the modes, however, further studies are required in order to provide a deeper understanding of the stabilization mechanisms. Example KBM mode structures for the elongated, triangular

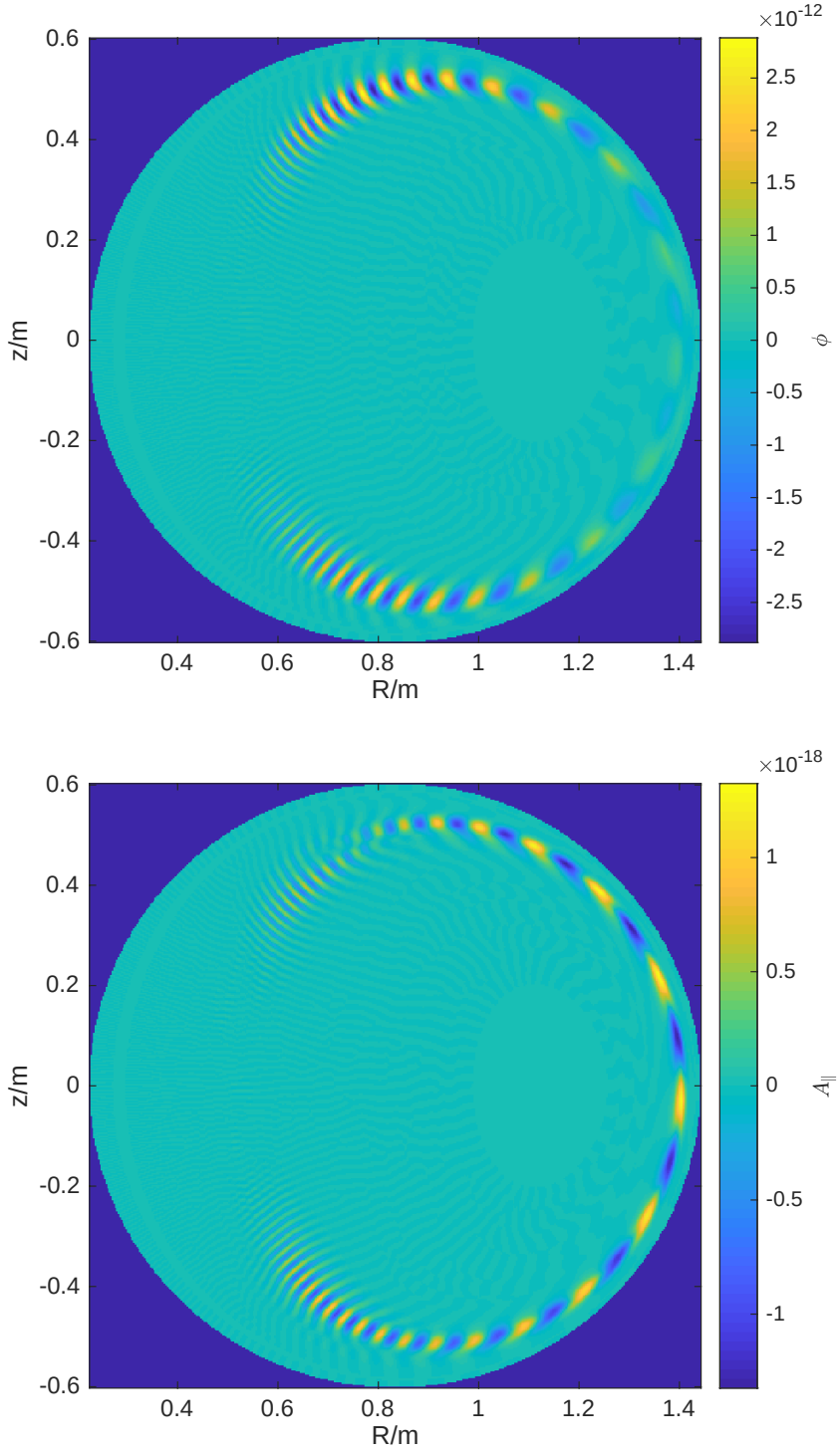

FIG. 18. Mode structures for the perturbed electrostatic ϕ (top) and parallel magnetic $A_{\|}$ (bottom) potentials in the (R, z) plane for the CMTM at $\beta_{\mathrm{e}} = 10\%$ for the $n = 20$ circular geometry case described in Section IV.

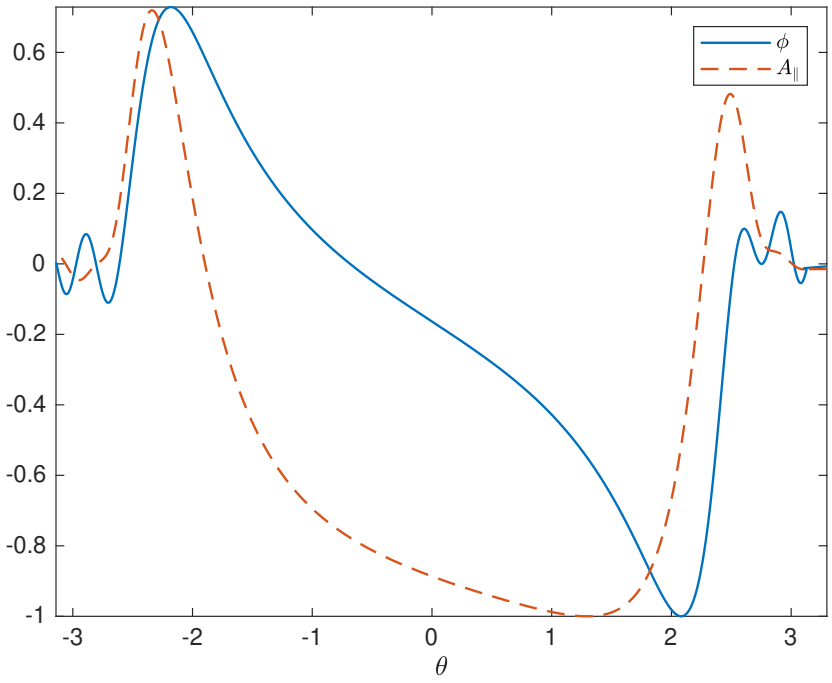

FIG. 19. Mode structures along a field line at the radial location where the mode peaks for the normalized perturbed electrostatic potential ϕ and normalized parallel magnetic potential $A_{\parallel}$ for the CMTM at $\beta_e = 10\%$ for the $n = 20$ circular geometry case described in Section IV, where θ is the geometric poloidal angle.

geometry case are shown in Figure 21.

Overall, both elongation and triangularity have significant stabilizing effects. This may be due to an increase in good-curvature[52] regions in the high-toroidicity configuration.

We now compare the results that included $\delta B_{\parallel}$ effects with the results that did not include $\delta B_{\parallel}$ effects. For all three geometries at low β_e, including $\delta B_{\parallel}$ effects has a relatively small effect, however, as β_e is increased, the effect of including $\delta B_{\parallel}$ effects is greater. The difference in growth rate between including $\delta B_{\parallel}$ effects and not including $\delta B_{\parallel}$ effects is greatest for the circular geometry case at high β_e. The difference for the elongated geometry case at high β_e is approximately 10%, and the difference for the elongated, triangular geometry case is approximately 30%. In general, including $\delta B_{\parallel}$ effects results in higher growth rates and real frequencies than when not including $\delta B_{\parallel}$ effects. This is in agreement with previous studies.[7,11–15,18,21,23,24]

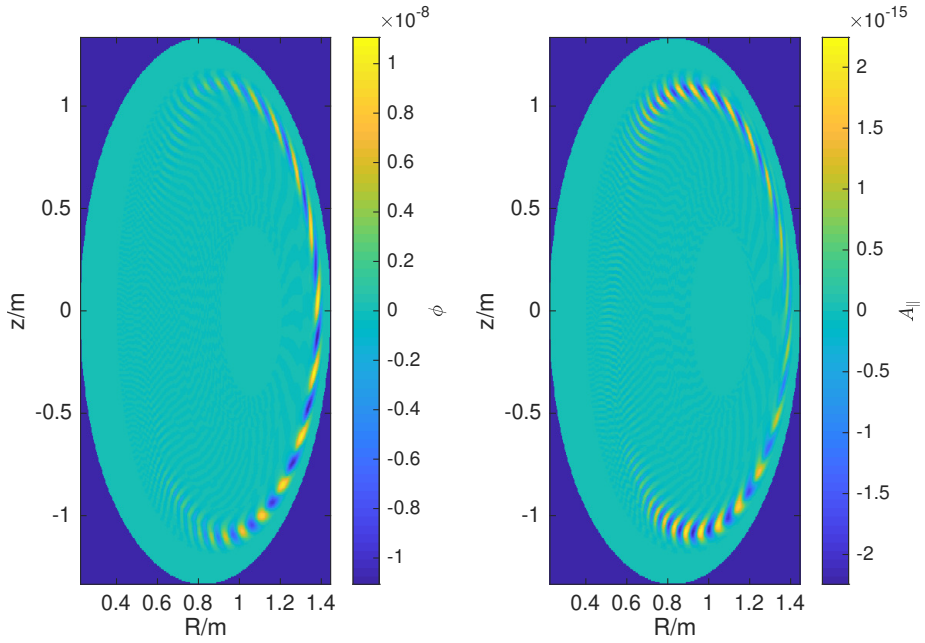

FIG. 20. Mode structures for the perturbed electrostatic ϕ (left) and parallel magnetic $A_{\|}$ (right) potentials in the (R, z) plane for the CTEM at $\beta_e = 15\%$ for the $n = 20$ elongated geometry case described in Section IV.

V. CONCLUSION

A workflow has been developed to perform scans over plasma β using profile-consistent magnetic equilibria with the global gyrokinetic PIC code XGC, without the inclusion of Coulomb collisions. This capability has been used in the cross-verification of an approximation for the inclusion of compressional magnetic perturbation effects between the global gyrokintic code XGC, and the global versions of the gyrokinetic codes GEM and GENE. XGC has then been used to study the effects of shaping on electromagnetic mode stability at NSTX aspect ratio and high plasma β. The plasma profiles that were used were based on standard CBC profiles. A toroidal mode number of $n = 20$ was used, where the electromagnetic modes appear to be strong.

When the plasma cross-sectional shape is circular, it is found that CMTMs are dominant, while the usual CTEMs are dominant in the low-β_e limit. When a level of elongation that is identical to that of NSTX discharge 132588 is added, the CMTMs are less dominant and the CMTM critical β_e[8] increases to the level of the experimental β_e, meaning that, with

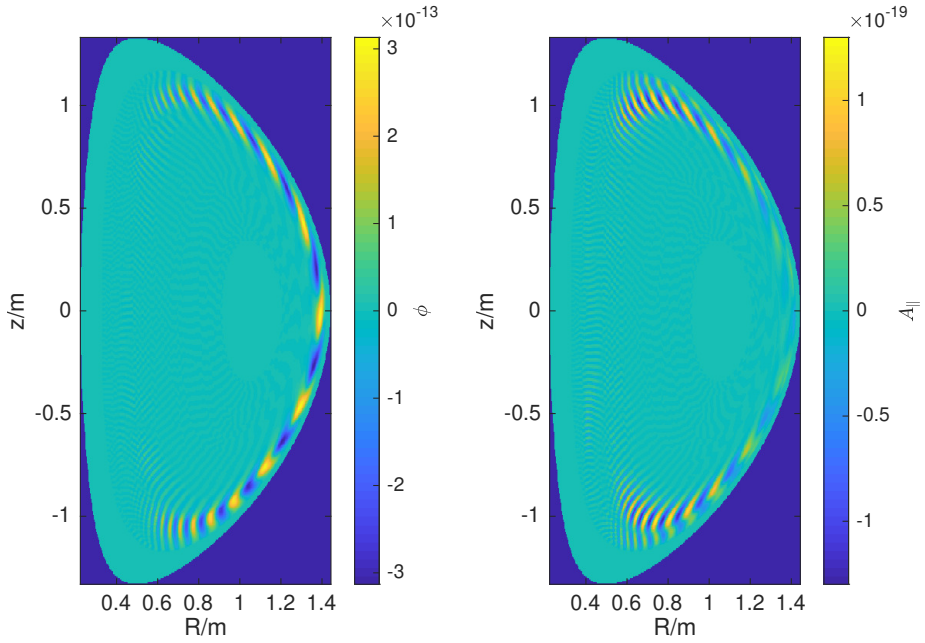

FIG. 21. Mode structures for the perturbed electrostatic ϕ (left) and parallel magnetic $A_{\|}$ (right) potentials in the (R, z) plane for the KBM at $\beta_e = 30\%$ for the $n = 20$ elongated, triangular geometry case described in Section IV.

elongation alone, CMTMs can be marginally unstable.

When a level of triangularity that is identical to that of NSTX discharge 132588 is added, CMTMs become stable, CTEMs become dominant at the experimental β_e range, and then transition to KBMs at or somewhat above the experimental β_e. However, the linear KBM growth rate becomes much lower than the value we are familiar with at the conventional aspect ratio; there is no sudden explosive growth rate as the ion-scale modes (CTEMs in this case) transition to KBMs. Thus, the present global gyrokinetic study does not provide evidence that KBMs are a limiting factor to the β_e or pressure gradient in the highly shaped, high-performance EP H-mode discharge 132588 studied in the present work.

The simplified compressional magnetic perturbation model has been shown to be valid for various cases at high aspect ratio (see Section III and References 18 and 21), however, this validity is yet to be confirmed at low aspect ratio, although future work and experimental evidence may be able to address this. In addition, the representation of CMTMs in this study may be limited due to the coarse radial resolution used in the simulations.

No dominant ITGs were observed in any of the low-aspect-ratio cases, which is consistent

with the expected stabilization effects due to reduced "bad-curvature" drive and strong Shafranov shift at low aspect ratio,[53,54] as well as EM stabilization effects.[55] Even though the profiles that were used in the shaping study are very different from those of NSTX discharge 132588, the absence of ITGs is also consistent with the observation that ion thermal transport in NSTX H-modes is typically observed to be described entirely by neoclassical transport,[56] that is to say, no anomalous transport or turbulent contributions are required.

ACKNOWLEDGEMENTS

The authors would like to thank the reviewers for their careful reading of this manuscript, as well as J. M. Canik, J. Dominski, S. E. Parker, and N. Kumar for fruitful discussions. This work was supported by the U.S. Department of Energy under contract number DE-AC02-09CH11466. The United States Government retains a non-exclusive, paid-up, irrevocable, world-wide license to publish or reproduce the published form of this manuscript, or allow others to do so, for United States Government purposes. This research used resources of the National Energy Research Scientific Computing Center (NERSC), a U.S. Department of Energy Office of Science User Facility located at Lawrence Berkeley National Laboratory, operated under Contract No. DE-AC02-05CH11231 using NERSC award FES-ERCAPm499.

DATA AVAILABILITY

The data that support the findings of this study are available in Reference 57, as well as from the corresponding author upon reasonable request.

AUTHOR DECLARATIONS

The authors have no conflicts to disclose.

REFERENCES

[1]S. M. Kaye, D. J. Battaglia, D. Baver, E. Belova, J. W. Berkery, V. N. Duarte, N. Ferraro, E. Fredrickson, N. Gorelenkov, W. Guttenfelder, G. Z. Hao, W. Heidbrink, O. Izacard, D. Kim, I. Krebs, R. L. Haye, J. Lestz, D. Liu, L. A. Morton, J. Myra, D. Pfefferle,

M. Podesta, Y. Ren, J. Riquezes, S. A. Sabbagh, M. Schneller, F. Scotti, V. Soukhanovskii, S. J. Zweben, J. W. Ahn, J. P. Allain, R. Barchfeld, F. Bedoya, R. E. Bell, N. Bertelli, A. Bhattacharjee, M. D. Boyer, D. Brennan, G. Canal, J. Canik, N. Crocker, D. Darrow, L. Delgado-Aparicio, A. Diallo, C. Domier, F. Ebrahimi, T. Evans, R. Fonck, H. Frerichs, K. Gan, S. Gerhardt, T. Gray, T. Jarboe, S. Jardin, M. A. Jaworski, R. Kaita, B. Koel, E. Kolemen, D. M. Kriete, S. Kubota, B. P. LeBlanc, F. Levinton, N. Luhmann, R. Lunsford, R. Maingi, R. Maqueda, J. E. Menard, D. Mueller, C. E. Myers, M. Ono, J.-K. Park, R. Perkins, F. Poli, R. Raman, M. Reinke, T. Rhodes, C. Rowley, D. Russell, E. Schuster, O. Schmitz, Y. Sechrest, C. H. Skinner, D. R. Smith, T. Stotzfus-Dueck, B. Stratton, G. Taylor, K. Tritz, W. Wang, Z. Wang, I. Waters, and B. Wirth, Nuclear Fusion **59**, 112007 (2019).

[2]J. E. Menard, S. Gerhardt, M. Bell, J. Bialek, A. Brooks, J. Canik, J. Chrzanowski, M. Denault, L. Dudek, D. A. Gates, N. Gorelenkov, W. Guttenfelder, R. Hatcher, J. Hosea, R. Kaita, S. Kaye, C. Kessel, E. Kolemen, H. Kugel, R. Maingi, M. Mardenfeld, D. Mueller, B. Nelson, C. Neumeyer, M. Ono, E. Perry, R. Ramakrishnan, R. Raman, Y. Ren, S. Sabbagh, M. Smith, V. Soukhanovskii, T. Stevenson, R. Strykowsky, D. Stutman, G. Taylor, P. Titus, K. Tresemer, K. Tritz, M. Viola, M. Williams, R. Woolley, H. Yuh, H. Zhang, Y. Zhai, and A. Z. and, Nuclear Fusion **52**, 083015 (2012).

[3]H. Meyer, I. G. Abel, R. J. Akers, A. Allan, S. Y. Allan, L. C. Appel, O. Asunta, M. Barnes, N. C. Barratt, N. B. Ayed, J. W. Bradley, J. Canik, P. Cahyna, M. Cecconello, C. D. Challis, I. T. Chapman, D. Ciric, G. Colyer, N. J. Conway, M. Cox, B. J. Crowley, S. C. Cowley, G. Cunningham, A. Danilov, A. Darke, M. F. M. D. Bock, G. D. Temmerman, R. O. Dendy, P. Denner, D. Dickinson, A. Y. Dnestrovsky, Y. Dnestrovsky, M. D. Driscoll, B. Dudson, D. Dunai, M. Dunstan, P. Dura, S. Elmore, A. R. Field, G. Fishpool, S. Freethy, W. Fundamenski, L. Garzotti, Y. C. Ghim, K. J. Gibson, M. P. Gryaznevich, J. Harrison, E. Havlíčková, N. C. Hawkes, W. W. Heidbrink, T. C. Hender, E. Highcock, D. Higgins, P. Hill, B. Hnat, M. J. Hole, J. Horáček, D. F. Howell, K. Imada, O. Jones, E. Kaveeva, D. Keeling, A. Kirk, M. Kočan, R. J. Lake, M. Lehnen, H. J. Leggate, Y. Liang, M. K. Lilley, S. W. Lisgo, Y. Q. Liu, B. Lloyd, G. P. Maddison, J. Mailloux, R. Martin, G. J. McArdle, K. G. McClements, B. McMillan, C. Michael, F. Militello, P. Molchanov, S. Mordijck, T. Morgan, A. W. Morris, D. G. Muir, E. Nardon, V. Naulin, G. Naylor, A. H. Nielsen, M. R. O'Brien, T. O'Gorman, S. Pamela, F. I. Parra, A. Patel, S. D. Pinches, M. N. Price,

C. M. Roach, J. R. Robinson, M. Romanelli, V. Rozhansky, S. Saarelma, S. Sangaroon, A. Saveliev, R. Scannell, J. Seidl, S. E. Sharapov, A. A. Schekochihin, V. Shevchenko, S. Shibaev, D. Stork, J. Storrs, A. Sykes, G. J. Tallents, P. Tamain, D. Taylor, D. Temple, N. Thomas-Davies, A. Thornton, M. R. Turnyanskiy, M. Valovič, R. G. L. Vann, E. Verwichte, P. Voskoboynikov, G. Voss, S. E. V. Warder, H. R. Wilson, I. Wodniak, S. Zoletnik, and R. Z. and, Nuclear Fusion **53**, 104008 (2013).

[4]J. Milnes, N. B. Ayed, F. Dhalla, G. Fishpool, J. Hill, I. Katramados, R. Martin, G. Naylor, T. O'Gorman, and R. Scannell, Fusion Engineering and Design **96-97**, 42 (2015), proceedings of the 28th Symposium On Fusion Technology (SOFT-28).

[5]J. A. Krommes, Annual Review of Fluid Mechanics **44**, 175 (2012).

[6]S. Ku, C. S. Chang, R. Hager, R. M. Churchill, G. R. Tynan, I. Cziegler, M. Greenwald, J. Hughes, S. E. Parker, M. F. Adams, E. D'Azevedo, and P. Worley, Physics of Plasmas **25**, 056107 (2018).

[7]E. A. Belli and J. Candy, Physics of Plasmas **17**, 112314 (2010).

[8]M. Coury, W. Guttenfelder, D. R. Mikkelsen, J. M. Canik, G. P. Canal, A. Diallo, S. Kaye, G. J. Kramer, and R. Maingi, Physics of Plasmas **23**, 062520 (2016).

[9]J. Chowdhury and B. F. McMillan, Plasma Physics and Controlled Fusion **63**, 075017 (2021).

[10]J. L. Peterson, R. Bell, J. Candy, W. Guttenfelder, G. W. Hammett, S. M. Kaye, B. LeBlanc, D. R. Mikkelsen, D. R. Smith, and H. Y. Yuh, Physics of Plasmas **19**, 056120 (2012).

[11]W. M. Tang, J. W. Connor, and R. J. Hastie, Nuclear Fusion **20**, 1439 (1980).

[12]M. Kotschenreuther, W. Dorland, Q. P. Liu, M. C. Zarnstorff, R. L. Miller, and Y. R. Lin-Liu, Nuclear Fusion **40**, 677 (2000).

[13]C. Bourdelle, W. Dorland, X. Garbet, G. W. Hammett, M. Kotschenreuther, G. Rewoldt, and E. J. Synakowski, Physics of Plasmas **10**, 2881 (2003).

[14]W. Guttenfelder, J. L. Peterson, J. Candy, S. M. Kaye, Y. Ren, R. E. Bell, G. W. Hammett, B. P. LeBlanc, D. R. Mikkelsen, W. M. Nevins, and H. Yuh, Nuclear Fusion **53**, 093022 (2013).

[15]J. M. Canik, W. Guttenfelder, R. Maingi, T. H. Osborne, S. Kubota, Y. Ren, R. E. Bell, H. W. Kugel, B. P. LeBlanc, and V. A. Souhkanovskii, Nuclear Fusion **53**, 113016 (2013).

[16]M. D. J. Cole, A. Mishchenko, A. Bottino, and C. S. Chang, Physics of Plasmas **28**, 034501 (2021).

[17]R. Hager, S. Ku, A. Y. Sharma, C. S. Chang, R. M. Churchill, and A. Scheinberg, Physics of Plasmas, submitted (2022).

[18]N. Joiner, A. Hirose, and W. Dorland, Physics of Plasmas **17**, 072104 (2010).

[19]G. Dong, J. Bao, A. Bhattacharjee, A. Brizard, Z. Lin, and P. Porazik, Physics of Plasmas **24**, 081205 (2017).

[20]H. L. Berk and R. R. Dominguez, Journal of Plasma Physics **18**, 31–48 (1977).

[21]R. E. Waltz and R. L. Miller, Physics of Plasmas **6**, 4265 (1999).

[22]J. Candy, Plasma Physics and Controlled Fusion **51**, 105009 (2009).

[23]J. P. Graves, D. Zullino, D. Brunetti, S. Lanthaler, and C. Wahlberg, Plasma Physics and Controlled Fusion **61**, 104003 (2019).

[24]J. P. Martin Collar, B. F. McMillan, S. Saarelma, and A. Bottino, Plasma Physics and Controlled Fusion **62**, 095005 (2020).

[25]T. Görler, X. Lapillonne, S. Brunner, T. Dannert, F. Jenko, F. Merz, and D. Told, Journal of Computational Physics **230**, 7053 (2011).

[26]S. C. Cowley, R. M. Kulsrud, and R. Sudan, Physics of Fluids B: Plasma Physics **3**, 2767 (1991).

[27]T. S. Hahm and W. M. Tang, PPPL Technical Report **2721** (1990).

[28]A. K. Swamy, R. Ganesh, J. Chowdhury, S. Brunner, J. Vaclavik, and L. Villard, Physics of Plasmas **21**, 082513 (2014).

[29]D. R. Hatch, M. Kotschenreuther, S. M. Mahajan, M. J. Pueschel, C. Michoski, G. Merlo, E. Hassan, A. R. Field, L. Frassinetti, C. Giroud, J. C. Hillesheim, C. F. Maggi, C. P. von Thun, C. M. Roach, S. Saarelma, D. Jarema, F. Jenko, and J. Contributors, Nuclear Fusion **61**, 036015 (2021).

[30]M. Kotschenreuther, X. Liu, D. Hatch, S. Mahajan, L. Zheng, A. Diallo, R. Groebner, J. Hillesheim, C. Maggi, C. Giroud, F. Koechl, V. Parail, S. Saarelma, E. Solano, A. Chankin, and and, Nuclear Fusion **59**, 096001 (2019).

[31]M. Fivaz, T. M. Tran, K. Appert, J. Vaclavik, and S. E. Parker, Phys. Rev. Lett. **78**, 3471 (1997).

[32]B. J. Sturdevant, S. Ku, L. Chacón, Y. Chen, D. Hatch, M. D. J. Cole, A. Y. Sharma, M. F. Adams, C. S. Chang, S. E. Parker, and R. Hager, Physics of Plasmas **28**, 072505

(2021).

[33]T. Görler, N. Tronko, W. A. Hornsby, A. Bottino, R. Kleiber, C. Norscini, V. Grandgirard, F. Jenko, and E. Sonnendrücker, Physics of Plasmas **23**, 072503 (2016).

[34]S. P. Hirshman and J. C. Whitson, The Physics of Fluids **26**, 3553 (1983).

[35]T. C. Luce, Plasma Physics and Controlled Fusion **55**, 095009 (2013).

[36]N. Marushchenko, Y. Turkin, and H. Maassberg, Computer Physics Communications **185**, 165 (2014).

[37]A. M. Dimits, Physics of Plasmas **17**, 055901 (2010).

[38]A. Y. Sharma and B. F. McMillan, Physics of Plasmas **22**, 032510 (2015).

[39]B. F. McMillan and A. Sharma, Physics of Plasmas **23**, 092504 (2016).

[40]A. Y. Sharma and B. F. McMillan, Journal of Plasma Physics **86**, 905860401 (2020).

[41]A. M. Dimits, G. Bateman, M. A. Beer, B. I. Cohen, W. Dorland, G. W. Hammett, C. Kim, J. E. Kinsey, M. Kotschenreuther, A. H. Kritz, L. L. Lao, J. Mandrekas, W. M. Nevins, S. E. Parker, A. J. Redd, D. E. Shumaker, R. Sydora, and J. Weiland, Physics of Plasmas **7**, 969 (2000).

[42]A. Brizard, Physics of Fluids B: Plasma Physics **4**, 1213 (1992).

[43]R. L. Miller, M. S. Chu, J. M. Greene, Y. R. Lin-Liu, and R. E. Waltz, Physics of Plasmas **5**, 973 (1998).

[44]R. Kleiber, R. Hatzky, A. Könies, A. Mishchenko, and E. Sonnendrücker, Physics of Plasmas **23**, 032501 (2016).

[45]Y. Chen and S. E. Parker, Journal of Computational Physics **220**, 839 (2007).

[46]F. Zhang, R. Hager, S.-H. Ku, C.-S. Chang, S. C. Jardin, N. M. Ferraro, E. S. Seol, E. Yoon, and M. S. Shephard, Engineering with Computers **32**, 285 (2016).

[47]C. S. Chang, S. Ku, P. H. Diamond, Z. Lin, S. Parker, T. S. Hahm, and N. Samatova, Physics of Plasmas **16**, 056108 (2009).

[48]R. Maingi, T. Osborne, M. Bell, R. Bell, D. Boyle, J. Canik, A. Diallo, R. Kaita, S. Kaye, H. Kugel, B. LeBlanc, S. Sabbagh, C. Skinner, and V. Soukhanovskii, Journal of Nuclear Materials **463**, 1134 (2015).

[49]R. Maingi, J. Canik, R. Bell, D. Boyle, A. Diallo, R. Kaita, S. Kaye, B. LeBlanc, S. Sabbagh, F. Scotti, and V. Soukhanovskii, Fusion Engineering and Design **117**, 150 (2017).

[50]J. Dominski, C. S. Chang, R. Hager, P. Helander, S. Ku, and E. S. Yoon, Journal of Plasma Physics **85**, 905850510 (2019).

[51]A. J. Brizard and T. S. Hahm, Rev. Mod. Phys. **79**, 421 (2007).

[52]A. H. Boozer, Rev. Mod. Phys. **76**, 1071 (2005).

[53]Y.-K. M. Peng and D. J. Strickler, Nuclear Fusion **26**, 769 (1986).

[54]G. Rewoldt, W. M. Tang, S. Kaye, and J. Menard, Physics of Plasmas **3**, 1667 (1996).

[55]J. Y. Kim, W. Horton, and J. Q. Dong, Physics of Fluids B: Plasma Physics **5**, 4030 (1993).

[56]S. M. Kaye, S. Gerhardt, W. Guttenfelder, R. Maingi, R. E. Bell, A. Diallo, B. P. LeBlanc, and M. Podesta, Nuclear Fusion **53**, 063005 (2013).

[57]"https://dataspace.princeton.edu/handle/88435/dsp018p58pg29j," (2022).